

NEAR-INFRARED DETECTION OF A SUPER-THIN DISK IN NGC 891

ANDREW SCHECHTMAN-ROOK^{1,2}, MATTHEW A. BERSHADY¹

Submitted to ApJ 2013 March 13; accepted 2013 June 21

ABSTRACT

We probe the disk structure of the nearby, massive, edge-on spiral galaxy NGC 891 with sub-arcsecond resolution *JHK_s*-band images covering $\sim \pm 10$ kpc in radius and ± 5 kpc in height. We measure intrinsic surface brightness profiles using realistic attenuation corrections constrained from near- and mid-infrared (*Spitzer*) color maps and three-dimensional Monte-Carlo radiative-transfer models. In addition to the well-known thin and thick disks, a super-thin disk with 60-80 pc scale-height—comparable to the star-forming disk of the Milky Way—is visibly evident and required to fit the attenuation-corrected light distribution. Asymmetries in the super-thin disk light profile are indicative of young, hot stars producing regions of excess luminosity and bluer (attenuation-corrected) near-infrared color. To fit the inner regions of NGC 891, these disks must be truncated within ~ 3 kpc, with almost all their luminosity redistributed in a bar-like structure 50% thicker than the thin disk. There appears to be no classical bulge but rather a nuclear continuation of the super-thin disk. The super-thin, thin, thick, and bar components contribute roughly 30%, 42%, 13%, and 15% (respectively) to the total *K_s*-band luminosity. Disk axial ratios (length/height) decrease from 30 to 3 from super-thin to thick components. Both exponential and sech^2 vertical SB profiles fit the data equally well. We find that the super-thin disk is significantly brighter in the *K_s*-band than typically assumed in integrated SED models of NGC 891: it appears that in these models the excess flux, likely produced by young stars in the super-thin disk, has been mistakenly attributed to the thin disk.

Subject headings: galaxies: spiral – galaxies: stellar content – galaxies: individual (NGC 891) – galaxies: structure – galaxies: photometry

1. INTRODUCTION

A knowledge of the three-dimensional mass distribution of spiral galaxy disks is critical to understanding galaxy formation and evolution. Unfortunately, kinematic measurements of rotation curves only provide the total (stellar disk + dark matter) mass distribution. Generally, this issue has been avoided by making the assumption that stellar disks contribute all of the mass governing the rotation curve at small radii (the “maximal disk hypothesis”, van Albada et al. 1985). However, the recent finding of significant disk submaximality (Westfall et al. 2011; Bershady et al. 2011) indicates that the maximal disk hypothesis is, at best, not universally applicable and, at worst, invalid. Additionally, the choice of low-inclination galaxies is necessitated by the methodology of these new mass-decomposition methods, making them insensitive to morphological determinations of individual disk components (if multiple disks exist).

Disk mass can also be probed independently of the total gravitational potential by measuring the amount of starlight present in a galaxy and converting it into mass via a mass-to-light ratio Υ_* . Traditionally Υ_* is found by fitting stellar population synthesis (SPS) models to the integrated galaxy light (Walcher et al. 2011). However, the values for Υ_* computed this way are depen-

dent on many significant assumptions, leading to large uncertainties in Υ_* (see Bershady et al. 2010a for a discussion). Additionally, any estimates of luminosity are dependent on attenuation from dust within the galaxy, which is known to be both clumpy and inclination dependent (see Schechtman-Rook et al. 2012a and references therein). Lastly, as these SPS models are created with the integrated light of a galaxy, they cannot distinguish between different stellar disks, the detailed parameters of which can be significant for estimates of the disk mass (Bershady et al. 2010a,b).

Observing edge-on galaxies presents the best conditions for the identification and characterization of multiple disks, as any projection effects are minimized. However, the effects of dust attenuation are also maximized in galaxies with this orientation. While not as significant an issue in low-mass galaxies, where the dust is not tightly concentrated into a narrow lane (Dalcanton et al. 2004) and some galaxies are within the *Hubble Space Telescope*’s range for resolved stellar population studies of the vertical structure (Seth et al. 2005), in high mass galaxies similar to the Milky Way (MW) determining disk structure near the midplane is a considerable challenge.

The problem of attenuation from the dust lanes of massive, edge-on galaxies is mitigated somewhat by observing in the infrared, where light is minimally absorbed by dust. Ideally observations would be taken in the mid-infrared (MIR), around 3-4 μm , where attenuation is at its minimum and just blueward of the point where thermal emission from cool dust begins to dominate the spectral energy distribution (SED). However, this spectral region contains several narrow emis-

¹ University of Wisconsin, Department of Astronomy, 475 N. Charter St., Madison, WI 53706; andrew@astro.wisc.edu

² Visiting Astronomer, Kitt Peak National Observatory, National Optical Astronomy Observatories, which is operated by the Association of Universities for Research in Astronomy, inc. (AURA) under cooperative agreement with the National Science Foundation

sion lines from non-thermal polycyclic aromatic hydrocarbon (PAH) molecules, as well as some continuum flux from very hot, small grains (Meidt et al. 2012). Additionally, to avoid the high opacity of the Earth’s atmosphere at these wavelengths, observations in the MIR must be taken on space-based telescopes, which places strict limitations on the size of their mirrors. Current-generation space-based telescopes with MIR capabilities, such as the *Spitzer Space Telescope* (Werner et al. 2004) and *Wide-field Infrared Survey Explorer* (Wright et al. 2010), have relatively poor ($>1''$) resolution, which is generally too coarse to resolve surface-brightness profiles very near the midplane in all but the closest galaxies (90 pc, roughly the scale height of the young disk in the MW (Bahcall & Soneira 1980), is $<1''$ at 20 Mpc). At these wavelengths the diffraction limit also starts to become a significant limiting factor on resolution: *Spitzer*, for example, has a diffraction limit of $\sim 1.2''$ at $4\mu\text{m}$.

Ground-based near-infrared (NIR; $\sim 0.7\text{--}2.3\mu\text{m}$) detectors have improved dramatically in recent years and now can rival optical detectors in resolution and noise characteristics (e.g. Kissler-Patig et al. 2008; Meixner et al. 2010). However, while PAH emission is no longer a concern, attenuation can still be significant; Xilouris et al. (1999) find a central edge-on K-band optical depth of ~ 3 for NGC 891, for example. Due to the higher resolution and lack of dust emission, however, the NIR is the best choice for detailed studies of stellar disk parameters near the midplane of massive galaxies.

Other researchers have turned to the NIR in order to reduce the dust-lane attenuation of edge-on spirals. Barnaby & Thronson (1992) fit the surface-brightness distribution of an H-band image of NGC 5907 with a single vertical disk component, while Rice et al. (1996) perform a similar fit to NGC 4565 in the K-band. Both studies follow Wainscoat et al. (1989) in assuming that even for edge-on galaxies the effects of dust attenuation in the NIR are minimal³, which may contribute to their difficulties in fitting the vertical profiles. More recently, Yoachim & Dalcanton (2006) fit 2D models to edge-on galaxies from a survey with FWHM resolution of $\sim 1''$ in the K_s -band (Dalcanton & Bernstein 2000). However, this survey is not local enough to resolve super-thin disks ($1'' \sim 300$ pc at the sample’s average Hubble flow distance of 67 Mpc) and is also deliberately biased towards low surface-brightness galaxies.

Aoki et al. (1991) do make an effort to correct for the effects of dust in K-band vertical surface brightness profiles of NGC 891. However, they model the dust as a foreground screen, as opposed to a more physically realistic (albeit more complex) intermixture of dust and starlight. Xilouris et al. (1999) use a smooth, axisymmetric distribution of dust and starlight to fit radiative transfer models to optical and infrared data on a small sample of nearby edge-on galaxies, including NGC 891. While comparable to or better than current space-based capabilities in the MIR, none of these studies have high enough resolution in the NIR to fully explore any disk components with scale-heights similar to the MW’s young, star-forming disk at heights where they are likely to dominate the vertical surface-brightness profile.

³ Barnaby & Thronson 1992 do make a small attempt to include some dust effects.

In this paper we present high-resolution ($< 1''$) NIR observations of NGC 891, a massive edge-on spiral galaxy often compared to the MW. As a relatively isolated system without significant signs of interaction in its starlight (although it contains significant amounts of extra-planar gas; Oosterloo et al. 2007), NGC 891 is an excellent test case for studies of passive disk evolution in massive galaxies.

We combine these NIR observations with 3-dimensional Monte Carlo radiative transfer (RT) models, based on prior studies of NGC 891 (Schechtman-Rook et al. 2012a,b), which employ fractally clumped dust and dust-enshrouded star-formation. We use these models to compute an attenuation correction that is both astrophysically realistic and specifically tailored to NGC 891. In order to obtain a wider color baseline for the attenuation correction, we use archival *Spitzer* IRAC (Fazio et al. 2004) 3.6 and $4.5\mu\text{m}$ data in complement to the NIR data. While these data have a larger pixel size than the NIR data the surface brightness is generally smoothly varying, and as such introduces only a small amount of error into the attenuation corrections while allowing for a much tighter correction even at high attenuation.

We then apply this correction to our data, allowing us to produce fully attenuation-corrected surface-brightness (SB) profiles of NGC 891 and for the first time investigate disk morphology near the midplane of a massive spiral galaxy outside of the MW.

This paper is organized as follows: In Section 2 we present our data and describe our reduction software. We then detail our approach to removing the attenuation in Section 3. Light profiles and two-dimensional fits to the data are presented in Section 4. We discuss our results in a broader context in Section 5, and make concluding remarks in Section 6. We assume a distance to NGC 891 of 9.5 Mpc, so $1'' = 46$ pc.

2. NEAR INFRARED IMAGING DATA

2.1. Ground-Based Observations

All observations were obtained with the WIYN⁴ 3.5 m telescope at Kitt Peak National Observatory during an observing run in October 2011. We used the WIYN High-resolution InfraRed Camera (WHIRC; Meixner et al. 2010) near-infrared imager, and took data in the broad-band J, H, and K_s filters. WHIRC has a $3'3$ field-of-view and $0'1$ pixel scale, which allows it to fully exploit the excellent seeing at WIYN (median seeing $\sim 0'7$).

A log of the observations is presented in Table 1. Three regions of NGC 891 (the center, along the major axis NE of the center, and along the major axis to the SW) were observed to provide coverage on both sides of the galaxy out to ~ 2.5 and 14 K-band thin disk scale-lengths and scale-heights, respectively (10 and 4.7 kpc; Xilouris et al. 1999). Enough overlap was left between these pointings to allow for combined mosaics to be produced. Multiple exposures were taken in each band at each pointing in a dither pattern (with offsets between dithers $\sim 15''$ for J and H and $25''$ for K_s) and averaged into a mosaic; the seeing estimates provided in Table 1 are for the image

⁴ The WIYN observatory is a joint facility of the University of Wisconsin-Madison, Indiana University, Yale University, and the National Optical Astronomy Observatory.

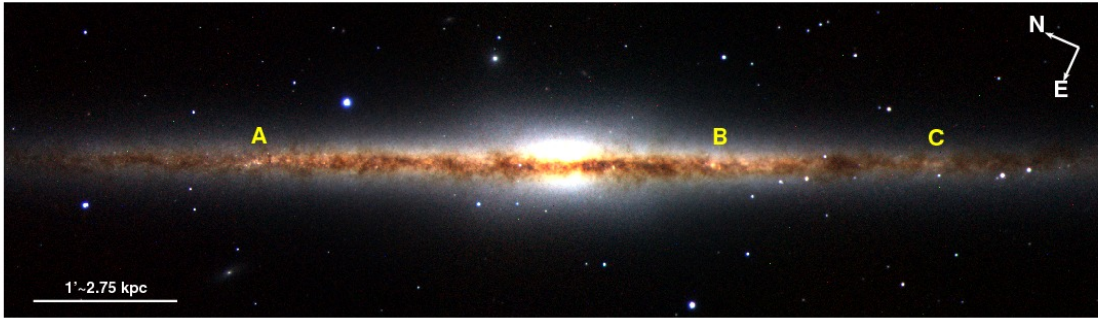


FIG. 1.— False-color RGB image of NGC 891, using the J (blue), H (green), and K_s (red) WHIRC data analyzed here. Labels (A, B, and C) are placed directly above three regions which appear to have enhanced, localized star formation on the side of the galaxy nearest to us. At the assumed distance, $1''$ corresponds to ~ 2.75 kpc. The image has a width of $7'.7 \sim 21.2$ kpc and a height of $2'.2 \sim 6.1$ kpc. The image is centered at $2:22:33.14, +42:20:57.5$, and has a position angle of 66.7° .

TABLE 1
LOG OF OBSERVATIONS

Filter	Date (UT)	Region	Exposure Time (s)		Seeing FWHM
			Individual	Total	
J...	2011 Oct 18	SW	80	640	$0''.6$
	2011 Oct 19	Center	80	640	$0''.9$
	2011 Oct 19	NE	80	640	$0''.9$
H...	2011 Oct 18	SW	80	640	$0''.8$
	2011 Oct 19	Center	80	640	$0''.7$
	2011 Oct 19	NE	80	640	$0''.5$
K_s ...	2011 Oct 18	SW	40	1080	$0''.9$
	2011 Oct 19	Center	40	1080	$0''.5$
	2011 Oct 19	NE	40	1080	$0''.5$

mosaics and come from Gaussian fits to foreground stars in the image using the IRAF⁵ task IMEXAM. In addition to the on-source data, we also intersperse dithers of a sky field to aid in sky background subtraction; the total exposure time of the sky dithers is of the same order as the total on-source exposure time. All observations were taken under photometric conditions. Mean seeing conditions were $0''.8$, $0''.67$, and $0''.63$ FWHM in J, H, and K_s , respectively. Full details of the data reduction can be found in Appendix A, and a false-color image of our final mosaics is shown in Figure 1.

2.2. *Spitzer* 3.6 and 4.5 μm Data

We downloaded “post-basic” calibrated data of NGC 891 from the *Spitzer* archive⁶ in the 3.6 and 4.5 μm IRAC channels. The images were inspected for defects. Very low level surface gradients were found across the images and surface-subtracted using the iterative method described in Schechtman-Rook & Hess (2012) and Martinsson et al. (2013). The resolution of the IRAC data is $\sim 1.8/\text{arcsec}$ (FWHM), twice as large as the worst quality JHK_s data. At these wavelengths, however, the surface-brightness distribution of NGC 891 is fairly smooth and slowly varying. Therefore we interpolate the IRAC data to match the WHIRC mosaics, assuming that oversampling the IRAC images does not contribute significant additional uncertainties to our computed atten-

uation correction and will not significantly degrade the resolution of the mosaics.

3. DUST CORRECTION

Estimating the dust extinction on sight-lines to individual stars inside the Milky Way is relatively easy because we can assume the dust is a foreground-screen (e.g. Cardelli et al. 1989). The task of estimating the internal extinction becomes far more difficult for external galaxies due to the complex interplay between stellar and dust geometries. For such systems the Calzetti et al. (1994) obscuration law is generally used. However, the Calzetti et al. (1994) law is designed for statistical studies of starbursts, not for detailed studies of individual galaxies and, moreover, does not take into account the inclination dependence of the obscuration law as seen in RT models (Matthews & Wood 2001; Pierini et al. 2004; Schechtman-Rook et al. 2012a) of disk galaxies. In the past, studies presenting surface photometry of edge-on spiral galaxies have avoided the midplane in their analysis (e.g. van der Kruit & Searle 1981; Barnaby & Thronson 1992; Barteldrees & Dettmar 1994; de Grijs & van der Kruit 1996) or used simplistic dust corrections (e.g. Wainscoat et al. 1989; Aoki et al. 1991; de Grijs et al. 1997; Yoachim & Dalcanton 2006). Here, we are able to focus on the midplane of NGC 891 using high-resolution NIR photometry and advanced RT models.

3.1. RT Models

Without knowing the 3D distribution of both dust and stars it is impossible to perfectly attenuation-correct images of NGC 891. However, we can compute a statistically accurate correction by modeling the dependence of color on the attenuation at multiple points in a simulated galaxy, which produces the average attenuation as well as the statistical uncertainty due to the varying distributions of stars and dust in different sight-lines. This correction is then broadly applicable for real galaxies with similar physical parameters (e.g. dust clumpiness) and orientations.

We base our models on the NGC 891 models of Bianchi (2008), with a bulge, two stellar disks (an old, thin disk and young super-thin disk), and a dust disk. We use the same physical scales and un-attenuated stellar SEDs for all components as in Bianchi (2008), however instead of individual molecular cloud-sized clumps we choose to

⁵ IRAF is distributed by the National Optical Astronomy Observatories, which is operated by the Association for Research in Astronomy, Inc., under cooperative agreement with the National Science Foundation.

⁶ AOR 3632384.

first place half of the total dust mass in fractal clumps. We choose not to model spiral structure: the rearrangement of dust and starlight might change the distribution of attenuation across the galaxy but should not effect the color resulting from a given amount of attenuation. Furthermore, the addition of spiral structure has a negligible effect on the integrated galaxy SED (Popescu et al. 2011); therefore ignoring spirality will not significantly alter the parameters of a given RT model. Both the percentage of dust in the fractal component as well as the details of the construction of the fractal grid follow from the median values for these parameters found in Schechtman-Rook et al. (2012a)’s modeling of NGC 891 - briefly, roughly 50% of the total dust mass is in clumps. In our models here the clumpy component is divided up into 130 fractal clumps. We choose to use the stellar emission parameters from Bianchi (2008) instead of this more recent work because Bianchi (2008) fit the entire SED of NGC 891 whereas Schechtman-Rook et al. (2012a) were most concerned about the clumpy nature of the dust in absorption and therefore only explored models without dust emission. The young super-thin disk component is placed proportionately to the dust density in each grid cell. In this way the super-thin disk is not only clumpy, but the clumpy stellar emission is co-spatial with the dust clumps. In order to fit the integrated SED both in the UV and the MIR, we find that we must also set a minimum dust density threshold below which there is zero emission from young stars. This threshold mimics the effect of having a gas surface density threshold for star formation (Martin & Kennicutt 2001).

The unattenuated stellar SEDs (again, following Bianchi 2008) are set to that of an Sb stellar SED for a galaxy with no dust from Floc & Rocca-Volmerange (1997). The light from stars with $M < 3 M_{\odot}$ is used as the input for the bulge and thin disk, while light from stars with $M > 3 M_{\odot}$ is assigned to the super-thin disk. The dust is included based on the prescription of Draine & Li (2007) with the mass fraction of PAHs $q_{PAH}=4.6\%$, with a size distribution to approximate $R_V=3.1$ from Weingartner & Draine (2001). For distribution in the model galaxy, the dust is split into three components: large grains, with grain size $a > 200\text{\AA}$, ultra-small (PAH dominated) grains, with $a < 20\text{\AA}$, and small grains, with sizes between those of the large and ultra-small grains. These three components make up 80.63%, 5.86%, and 13.51% of the total dust mass in a given voxel (volume pixel), respectively. This combination of physical parameters we designate as Model A, with the full set of parameters used to create the model given in Table 2.

As seen in Table 2, the super-thin disk of the model has a scale-length double the size of the thin disk’s scale-length but a scale-height half as large as for the thin disk. The thin disk has an axial ratio $\frac{h_R}{h_z} = 10$, common for spiral galaxies (Bershady et al. 2010b), while the super-thin disk has a much larger $\frac{h_R}{h_z} = 40$. However, due to the minimum dust density threshold and the addition of clumpiness, the axial ratio of the super-thin disk has less physical meaning than for the thin disk: at large distances from the center of the galaxy and/or the mid-plane the super-thin disk will be essentially truncated. The physical parameters of the thin disk and dust com-

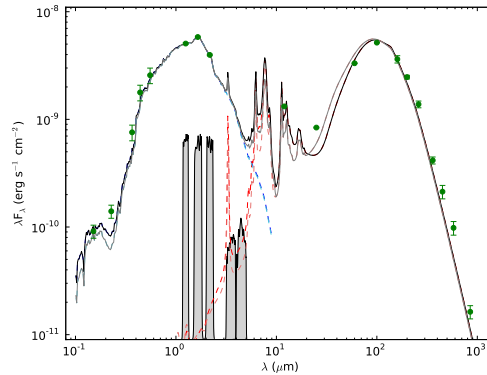


FIG. 2.— Comparison of the integrated SEDs of the two RT models used in this work. Light emitted from stars (directly and scattered) is shown in blue (cyan), while light emitted from dust (again, both directly and scattered) is shown in red (pink) for Model A (B). Total emission is shown in black for Model A and gray for Model B. The model truncates the stellar emission at $10 \mu\text{m}$; at longer wavelengths stellar emission contributes negligibly to the total flux. Green points show observational data for NGC 891 (Bianchi 2008). Gray shaded regions schematically illustrate the filter response curves of (from left to right): WHIRC J, H, and K_s ; IRAC $3.6\mu\text{m}$ and $4.5\mu\text{m}$.

ponent are based on the results of Xilouris et al. (1999). Popescu et al. (2011) take a similar approach, basing dust and thin disk parameters on Xilouris et al. (1999), but they choose a super-thin disk scale-height based on that found in the MW. We also note that Popescu et al. (2011) have an extra component of diffuse dust with the same scale parameters as the super-thin disk.

For the model used here we mapped a $100\times 100\times 100$ cell Cartesian grid to a $40\times 40\times 5$ kpc volume, where the 5 kpc dimension represents vertical height above and below the disk⁷. We chose to employ a rectangular grid rather than a cubical one to properly sample the vertical extent of the dust grid, which (as shown in Table 2) has a scale-height in our model of only 200 pc. In our previous work (Schechtman-Rook et al. 2012a), we used a RT code that only tracked scattering and absorption of photons emitted at a specific wavelength. The RT is performed by the HYPERION software package (Robitaille 2011), which computes the full SED of a model. HYPERION uses an iterative scheme to compute the dust temperature, and we use 100 million photon packets per iteration (an average of 100 photon packets per grid cell) for both for the temperature calculation iterations and to produce SEDs and images. We compare the output SED of the model to data in Figure 2. While the model has difficulty reproducing the mid-IR features associated with PAH emission and photo-dissociation regions, Bianchi (2008) indicate that this is likely due to a resolution effect in our models. Regardless of the reason for this discrepancy we are most concerned about the SED between $1 < \lambda (\mu\text{m}) < 5$, where the model appears to fit the data well.

3.2. Correction Procedure

To correct for the effects of dust on star-light we ran the model (described in Section 3.1) twice: once with

⁷ Each cell therefore has physical dimensions of $400\times 400\times 50$ pc. For comparison, assuming a distance to NGC 891 of 9.5 Mpc, the IRAC resolution is ~ 80 pc while the WHIRC resolution is ~ 40 pc.

TABLE 2
RT MODEL PARAMETERS

Parameter	Model A	Model B	Units
Bulge bolometric luminosity	1.8×10^{10}	1.8×10^{10}	L_{\odot}
Thin disk bolometric luminosity	4.2×10^{10}	3.9×10^{10}	L_{\odot}
Super-thin disk bolometric luminosity	2.8×10^{10}	2.8×10^{10}	L_{\odot}
Bulge effective radius	1.0	1.0	kpc
Bulge axial ratio b/a	0.6	0.6	—
Thin disk scale-length	4.0	4.0	kpc
Super-thin disk scale-length	8.0	8.0	kpc
Thin disk scale-height	0.4	0.4	kpc
Super-thin disk scale-height	0.2	0.2	kpc
Dust disk central density	3.6×10^{-26}	3.6×10^{-26}	g cm^{-3}
Dust disk scale-length	8.0	8.0	kpc
Dust disk scale-height	0.2	0.2	kpc
Dust clumping fraction	0.5	0.5	—
Number of largest-scale clumps	130	130	—
Dust density threshold for super-thin disk	3.4×10^{-27}	3.4×10^{-27}	g cm^{-3}

and once without any dust. We produced images in J, H, K_s , $3.6\mu\text{m}$, and $4.5\mu\text{m}$ for both model runs at the inclination of NGC 891 (89.7° , Xilouris et al. 1999). The attenuation A_{λ}^e at any given pixel is then simply

$$A_{\lambda}^e = -2.5 \log\left(\frac{F_{\lambda}}{F_{\lambda,nd}}\right), \quad (1)$$

where F_{λ} is the flux of the model with dust and $F_{\lambda,nd}$ is the flux of the model without dust. Note that we use ‘attenuation’ here broadly to include the threefold effects of dust: absorption, scattering, **and** emission. The latter is of particular importance moving into the MIR.

As can be seen Figure 2 (and will be discussed again in Section 3.3), there is a very strong, narrow PAH feature which lies within the IRAC $3.6\mu\text{m}$ bandpass. The $4.5\mu\text{m}$ filter, on the other hand, has no discrete dust components, although it is somewhat affected by continuum dust emission. We find that dust emission contributes 12% and 9% of the total integrated $3.6\mu\text{m}$ and $4.5\mu\text{m}$ model flux, respectively. Local values, along sight-lines involving dust clumps, are likely higher: Meidt et al. (2012) find ranges of 5-13% contamination at $3.6\mu\text{m}$ in the integrated light of *Spitzer* Survey of Stellar Structure in Galaxies (S^4G) targets but local amounts around 20% in star-forming regions. Therefore, based on the reduced contamination from dust emission at $4.5\mu\text{m}$ as well as the fact that it provides a larger wavelength baseline for other attenuation effects (absorption and scattering), we expect that the $4.5\mu\text{m}$ data will be more useful for estimating the NIR attenuation than the $3.6\mu\text{m}$ data.

With these considerations in mind we inspected the relationship between color and K_s -band attenuation of the model (Figure 3). An ideal attenuation correction metric would have both a tight and steep relationship between attenuation and color — i.e., a small error in color leads to a small error in the estimated attenuation. The J- and H- K_s corrections both have very small slopes at $A_{K_s}^e \gtrsim 0.75$ mag, making them poor choices for use as attenuation correctors. All NIR-IRAC colors (NIR- $4.5\mu\text{m}$ colors are shown in Figure 3, but the trends are very similar for NIR- $3.6\mu\text{m}$ colors) have similar slopes at $A_{K_s}^e \gtrsim 0.75$ of ~ 1 mag in color per mag in attenuation, which indicates that either the attenuation in the $4.5\mu\text{m}$ band is slowly varying or dust emission is, on aver-

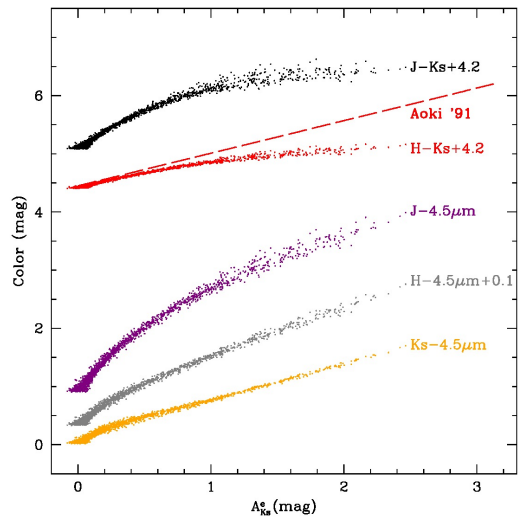


FIG. 3.— Colors as a function of K_s -band attenuation for Model B. Some colors have been offset (noted in the labels) to improve clarity. Points denote projected model pixels at edge-on inclination. Each pixel is 0.4×0.05 kpc (radius \times height), integrated over the 40 kpc line of sight in depth. The dashed red line shows the attenuation correction formula from Aoki et al. (1991), using H- K_s color.

age, offsetting the light losses due to attenuation at that wavelength.

While the NIR-IRAC colors have similar responses to increasing attenuation, the K_s - $4.5\mu\text{m}$ (also K_s - $3.6\mu\text{m}$) color clearly has the least scatter in the relationship. This is likely due to two factors: the K_s -band has less dust attenuation than either J or H, and that K_s is significantly redward of the Wein peak for even the coolest stars, which makes the K_s -IRAC color insensitive to the effects of different stellar populations. This feature is especially critical because it means that the assumptions we made about the parameters of the super-thin disk in Section 3.1 will not bias our results. Indeed, the attenuation corrections we produce use data at all positions in the model galaxy, and show a single trend applicable across the entire disk. For these reasons and those given concerning MIR dust contamination earlier in this Section, we choose to use the K_s - $4.5\mu\text{m}$ color to correct the

attenuation. We take the $1\text{-}\sigma$ error on the attenuation correction in $A_{K_s}^e$ and propagate that with the errors on the data to compute the final errors for the corrected surface-brightness images.

3.3. Multiple Dust Distributions

To test the applicability of Model A we overlaid color-color profiles of the model on the data and checked for discrepancies. We compared the colors as a function of both R and z to isolate any trends with position. A sample set of $K_s\text{-}3.6\mu\text{m}$ versus $J\text{-}K_s$ color-color distributions is shown in Figure 4; $K_s\text{-}4.5\mu\text{m}$ versus $J\text{-}K_s$ distributions are shown in Figure 5.

At large distances from the midplane (high z values), both the model and the data trend toward $K_s\text{-}3.6\mu\text{m}$ and $K_s\text{-}4.5\mu\text{m}$ colors of zero and $J\text{-}K_s$ colors of ~ 1 mag. The $K_s\text{-}IRAC$ color is a result of even the coolest stars being on the Rayleigh-Jeans tail in those spectral regions — the slopes of all stars are self-similar at these wavelengths, so Vega colors go to zero. We note that the large $J\text{-}K_s$ color implies the presence of very cool stars — a $J\text{-}K_s$ color of 1 mag is as red as the coldest dwarf in Bessell & Brett (1988). If the NIR light at these heights is dominated by giants, the $J\text{-}K_s$ color is roughly equivalent to a M2III star or an O-rich AGB with $T_{\text{eff}} \sim 3500$ K (Lançon & Mouhcine 2002).

It is also evident that at small height Model A fails to reproduce the colors of the data; model colors are increasingly too red in $K_s\text{-}3.6$ and $K_s\text{-}4.5$ when $z \lesssim 0.5$ kpc. Properly modeling the colors at $z < 0.5$ kpc is crucial, as the midplane is where attenuation from dust is the strongest **and** any signal from a super-thin disk component would be most apparent. While there is better overlap when using the $K_s\text{-}4.5\mu\text{m}$ color (top panel of Figure 5), Model A still produces redder $K_s\text{-}4.5\mu\text{m}$ colors than the data.

The culprit for the discrepancy in the colors appears to be an excess of PAH line emission in the model, as seen in Figure 2: there is a weak emission line at $\sim 3.5\mu\text{m}$ which falls within the IRAC $3.6\mu\text{m}$ bandpass, while the wings of several lines contribute to the flux in the $4.5\mu\text{m}$ band. There are (at least) two possible reasons for this discrepancy. The first is that there are fewer PAHs relative to other grain sizes near the midplane of NGC 891. Reducing the amount of PAHs decreases the total $3.6/4.5\mu\text{m}$ flux, increasing the $K_s\text{-}3.6/4.5\mu\text{m}$ color without affecting the $J\text{-}K_s$ color. Lowered PAH levels near the midplane could be the result of PAH grain destruction in high density areas, similar to what is seen in the MW (e.g. Povich et al. 2007). On the other hand there is also empirical evidence that, contrary to what is frequently assumed in dust models (including the model used here), the extinction law flattens in the MIR (Indebetouw et al. 2005; Zasowski et al. 2009). Flattening the extinction law for the IRAC bands would also have the effect of reducing the $K_s\text{-}3.6/4.5\mu\text{m}$ color at higher attenuations while leaving the NIR colors unchanged.

A full investigation of why a MW dust model has difficulty producing proper $K_s\text{-}3.6/4.5\mu\text{m}$ colors is beyond the scope of this work, given that we are merely concerned with computing a proper attenuation correction rather than conclusively determining the root cause of the attenuation. For simplicity, we choose to adjust the PAH levels in high density regions instead of changing the entire extinction law. Therefore we ran a second RT

model with two prescriptions for the fraction of different sized dust grains. In this new model (called Model B) voxels with dust densities $\leq 3.4 \times 10^{-27}$ g cm^{-3} are weighted 15% for ultra-small grains, 10% for small grains, and 75% for large grains, while high-density voxels use the following breakdown of grain sizes: 1% ultra-small grains, 35% small grains, and 64% large grains. All other quantities are held constant save the bolometric luminosity of the thin disk, which is decreased by $\sim 7\%$. These changes were made empirically by eye to better reproduce the IR colors of the data while still accurately fitting the integrated SED. The SED of Model B is shown alongside that of Model A in Figure 2, and color-color $K_s\text{-}3.6/4.5\mu\text{m}$ versus $J\text{-}K_s$ profiles are shown in the bottom panel of Figures 4 and 5.

Model B's SED has only 9% and 6% of the total $3.6\mu\text{m}$ and $4.5\mu\text{m}$ flux contributed by dust emission, generally better replicates the color distribution of NGC 891 than Model A. There are still some minor discrepancies between the data and the model in the MIR, however, which are shown in Figure 6. The model $3.6\mu\text{m}\text{-}4.5\mu\text{m}$ color is systematically bluer than the data. Near the midplane this is largely caused by the mismatch in the $3.6\mu\text{m}$ flux as discussed earlier, but at large heights some of the discrepancy arises from the model being slightly too faint at $4.5\mu\text{m}$ (visible in the bottom panels of both models in figure 5). This mismatch is $\lesssim 0.08$ mag, which implies that the y-intercepts of the attenuation correction formulae in Appendix C should be shifted by approximately that amount. The systematic error resulting from this mismatch will therefore be at the $\lesssim 8\%$ level, which should only impact flux measurements and (as will be seen later) does not have a significant effect on any of our conclusions. While the $3.6\mu\text{m}$ model flux does match the data at large heights, due to the aforementioned significant mismatch in dust-obscured regions we still consider the $4.5\mu\text{m}$ flux as more reliable for this purpose, systematic error notwithstanding. We will investigate ways to improve our input SEDs for future publications, but for now we will focus on demonstrating the rest of our methodology on NGC 891.

Functionally, adjusting the dust distribution decreases the reddening in the $K_s\text{-}IRAC\mu\text{m}$ color while leaving $J\text{-}K_s$ essentially unchanged. In addition to the systematic error in intrinsic MIR color, to have some leverage on our systematic uncertainty caused by our imperfect knowledge of the dust distribution we generally perform subsequent analyses with **both** models, using only Model B when we do not expect to see different responses to analysis from the two models and the savings in computation time is significant.

3.4. Attenuation Fits

The exact behavior of the attenuation as a function of color will be different in each bandpass, so we fit A_λ^e separately for J, H, and K_s . Fitting the attenuation from the RT models is non-trivial, largely because at low A_λ^e the slope of the attenuation curve changes significantly while at large attenuations the function becomes linear. This problem is compounded by the dearth of model data at very high attenuations. These factors lead to poor fits of single polynomial functions, especially at large A_λ^e . To deal with this issue we employ piecewise fits of the attenuation curve. Details of our method and the formulae

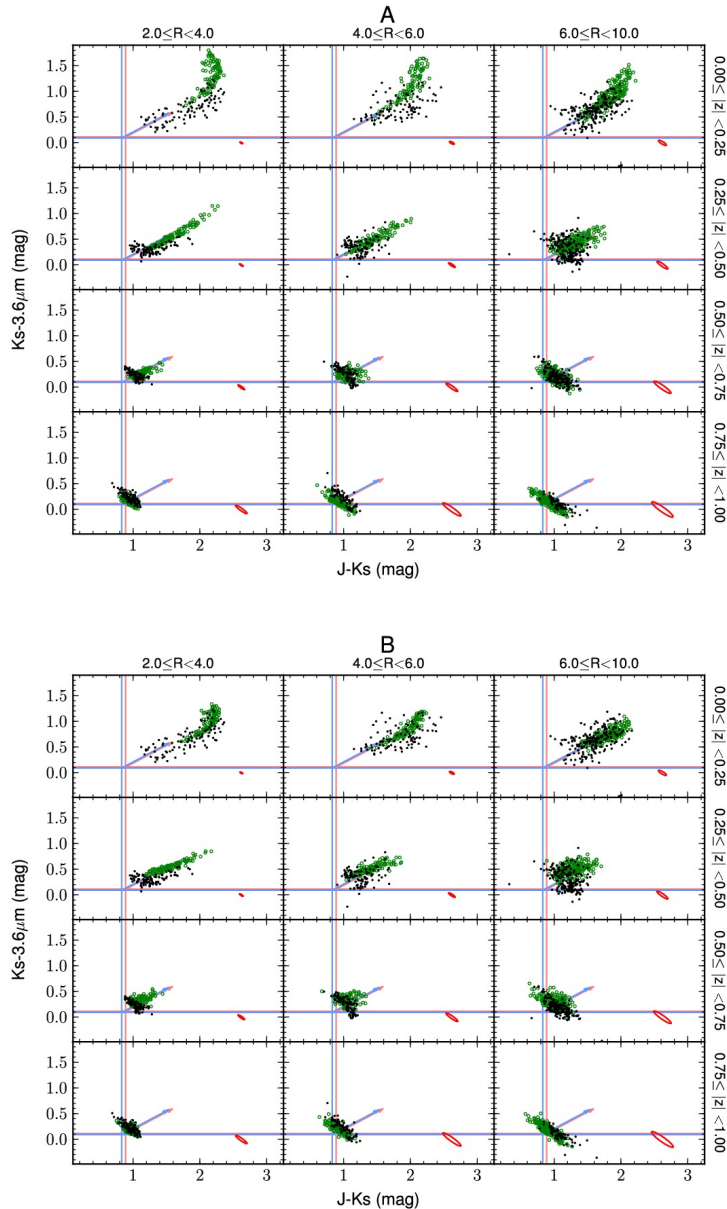


FIG. 4.— K_s - $3.6\mu\text{m}$ versus J - K_s color-color diagrams of Models A (top) and B (bottom) compared to the WHIRC/IRAC data in bins of R and z (given on the top and right axes). Model pixels are shown as open green points, while data pixels are black filled points. The data have been resampled to match the resolution of the model (400×50 pc). The red ellipses in the lower right of each panel represent 95% confidence error ellipses for the data. The model (green) pixels have been perturbed by random numbers drawn to match the error distribution in the data. The light red (light blue) lines show the intrinsic colors of the old (young) RT model input stellar SEDs, while the arrows approximate the reddening vector at modest ($A_{K_s}^e \sim 0.5$ mag) attenuation. At $A_{K_s}^e \gtrsim 1$ this vector becomes steeper because the J - K_s color index saturates before the K_s - $3.6\mu\text{m}$ colors.

for the resulting fits are shown in Appendix C.

The attenuation fits are plotted against the model data in Figure 7. In all cases it is apparent that the model trends are well fit. In Figure 7 we also compare the fits between Models A and B. At low attenuations Model B has much more complex behavior, although for all three bands the two models are within ~ 0.1 mag of each other in A_λ^e . At large attenuations the attenuation relations have very similar slopes but are offset from each other by about 0.3 mag in J , H , and K_s . Model B has more extinction at a given K_s - $4.5\mu\text{m}$ color than Model A, for K_s - $4.5\mu\text{m} \gtrsim 0.5$ mag. The difference in behavior between

the models at large values of K_s - $4.5\mu\text{m}$ arises because the depletion of PAH grains in Model B acts to lower the amount of line/continuum emission from dust at ~ 5 - $6\mu\text{m}$, the tail of which is blue enough to affect the $4.5\mu\text{m}$ IRAC band. The attenuation in the K_s -band, however, is not strongly affected by changes in PAH densities and therefore remains essentially constant. The result is that Model B has bluer K_s - $4.5\mu\text{m}$ colors for a given A_λ^e , seen in Figure 7. This also indicates that Model A overpredicts the $4.5\mu\text{m}$ surface brightness near the midplane by ~ 0.3 mag arcsec $^{-2}$.

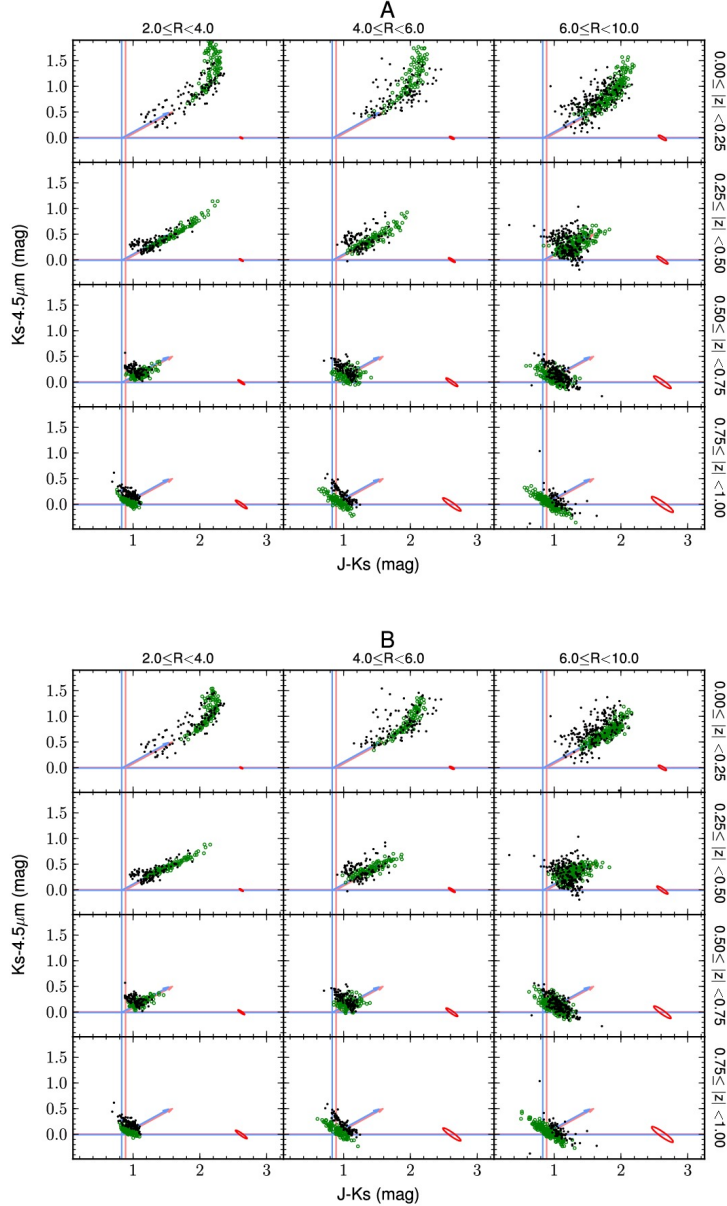


FIG. 5.— $K_s-4.5\mu\text{m}$ versus $J-K_s$ color-color diagrams comparing models to data. Color-coding as in Figure 4.

3.5. Comparison with Previous Attenuation Corrections

Assuming a MW extinction law and a foreground screen of dust, Aoki et al. (1991) correct their K-band emission by the formula

$$K_c = K_r - \frac{(H - K) - 0.25}{0.56}, \quad (2)$$

where K_r is the uncorrected K-band surface brightness and K_c is the corrected K-band surface brightness. As the reddest filter and therefore the data least likely to be affected by errors in the attenuation correction, we follow Aoki et al. (1991) and focus on our K_s -band data. We show the uncorrected K_s data along with corrected K_s profiles in Figure 8 on both sides of NGC 891 at 3, 5, 7, and 9 kpc in radius. We plot the vertical pro-

files at these positions because they show data at high S/N while avoiding bulge contamination, and are representative of the profiles at all radii. While the K and K_s -bands are not identical, we use the Aoki et al. (1991) attenuation correction on our data to obtain a schematic understanding of the differences between it and our RT methodology.

We find that generally both dust models in this work have larger peak attenuation than the Aoki et al. (1991) correction. Model A is on average brighter by ~ 0.16 mag, while Model B is brighter by ~ 0.33 mag. This discrepancy is likely due to the saturation of the $H-K_s$ color at large optical depths (Matthews & Wood 2001 and see Figure 3), which we are less sensitive to since we are using $K_s-4.5\mu\text{m}$ color and models that accurately represent this effect. Additionally, while the attenuation corrected vertical profiles of both Model A and Model B

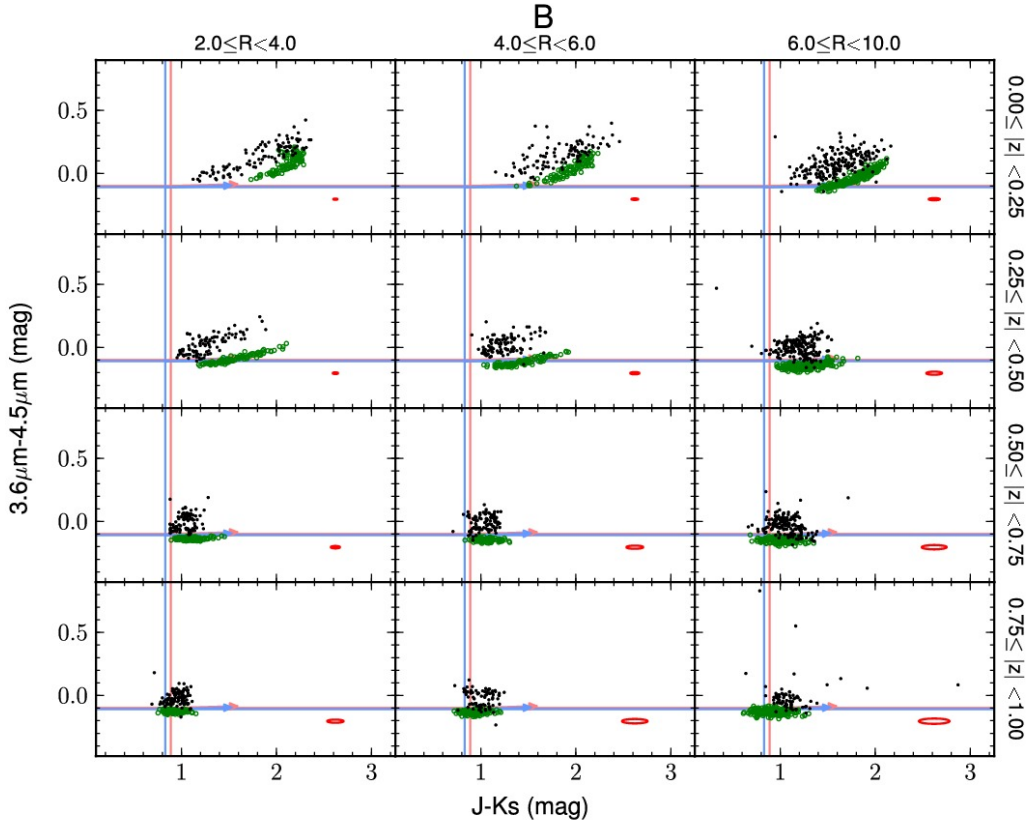


FIG. 6.— $3.6\mu\text{m}-4.5\mu\text{m}$ versus $J-K_s$ color-color diagrams comparing Model B to data. Color-coding as in Figure 4.

peak at a relatively consistent location at all radii, the peak of the Aoki et al. (1991) dust corrected data has much more variation (especially visible at 5 and 9 kpc). Our two RT models are very similar to each other, but (as predicted by Figure 7) the model with a PAH-depleted grain size distribution in high-density regions (Model B) leads to larger inferred A_λ^e for a given $K_s-4.5\mu\text{m}$ color than in Model A, resulting in a brighter corrected μ_{K_s} .

4. RESULTS

A false color JHK_s image of the central portion of the dust-corrected galaxy (using Model B) is shown in Figure 9, compared to the rescaled image before attenuation correction and the IRAC $4.5\mu\text{m}$ image. The central bulge region can now be clearly seen in the midplane. Additionally, while the majority of the dust-corrected image is smoothly varying, in several places (marked on Figure 9) there appear to be regions of slightly enhanced flux. These regions clearly correspond to areas with excess flux in the IRAC $4.5\mu\text{m}$ image, indicating that they are real flux overdensities and not artifacts of the attenuation correction process. These are likely candidates for star-forming regions. While parts of the three regions are visible as bright point-source knots of light even before attenuation correction (most easily visible in Figure 1), the true NIR projected size of these areas is only revealed after attenuation correction.

In general, the remarkable similarity between the morphology in the attenuation-corrected K_s image and the IRAC $4.5\mu\text{m}$ image is a confirmation that our correction

method is accurate. This similarity is not tautological since the relation between attenuation and color is based on the RT-model predictions and not the data.

4.1. Radial and Vertical Profiles with and without Dust Correction

We show NGC 891's JHK_s radial surface brightness profile along the major axis (i.e. $z=0$) un-corrected for dust attenuation in Figure 10. The vertical bin size is $0.9''$ or ~ 40 pc. The radial profiles with dust are very similar to those shown in Figure 9 of Aoki et al. (1991), except that our data shows a distinct bump in all bands at ~ 3 kpc on the SW side while they only see that feature in H and K. The reason for this discrepancy is unclear, but it indicates that this 3 kpc feature is a stellar over-density, not a dusty spiral arm as hypothesized by Aoki et al. (1991). We also present un-corrected $J-K_s$ and $H-K_s$ major axis color profiles in the left panel of Figure 11. The $J-K_s$ profile seems to show a weak trend towards bluer colors with increasing radius, but there is significant scatter. The $H-K_s$ profile shows a similarly weak trend. No color trend is visible as a function of radius when using attenuation corrected profiles (right panel of Figure 11). There is also an asymmetry between the NE and SW colors of NGC 891 around $R\sim 3$ kpc, in the same position with the apparent stellar overdensity discussed previously in Figure 10.

Our major axis radial profiles also show the northeast side of NGC 891, which was not shown in Aoki et al. (1991) due to noise issues in the H band on their detec-

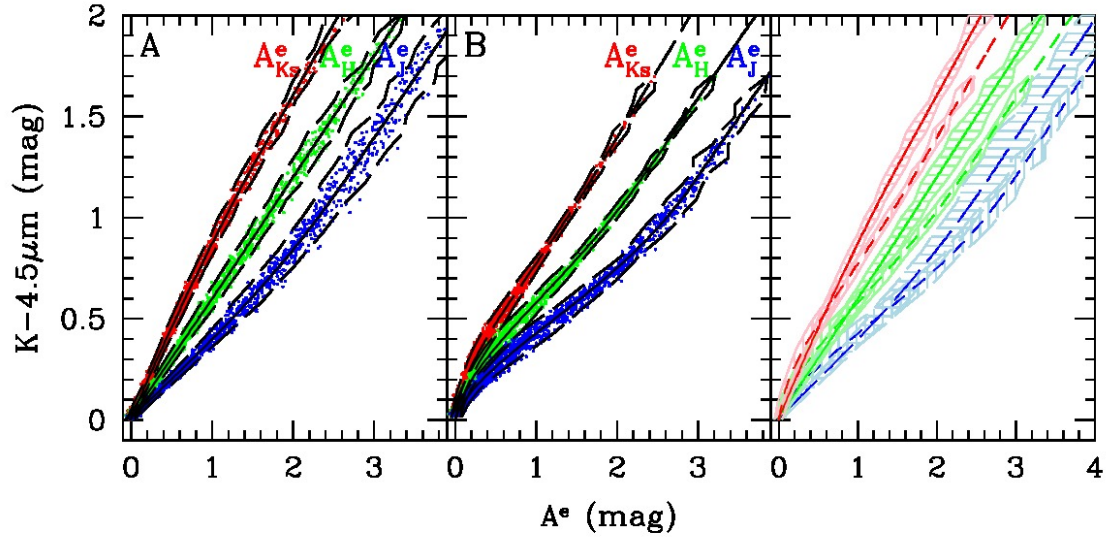


FIG. 7.— Attenuation corrections for all three NIR bands. On the left and middle panels points are individual projected model pixels (as in Figure 3), while the black solid lines show the piecewise fits to the ‘data’. Dashed black lines denote 95% confidence limits in the distribution of A_{λ}^e at a given model color. Left panel: Model A. Middle panel: Model B. The rightmost panel compares the best fitting attenuation correction from Model A (solid lines) and Model B (dashed lines), with shaded regions denoting the 2σ errors.

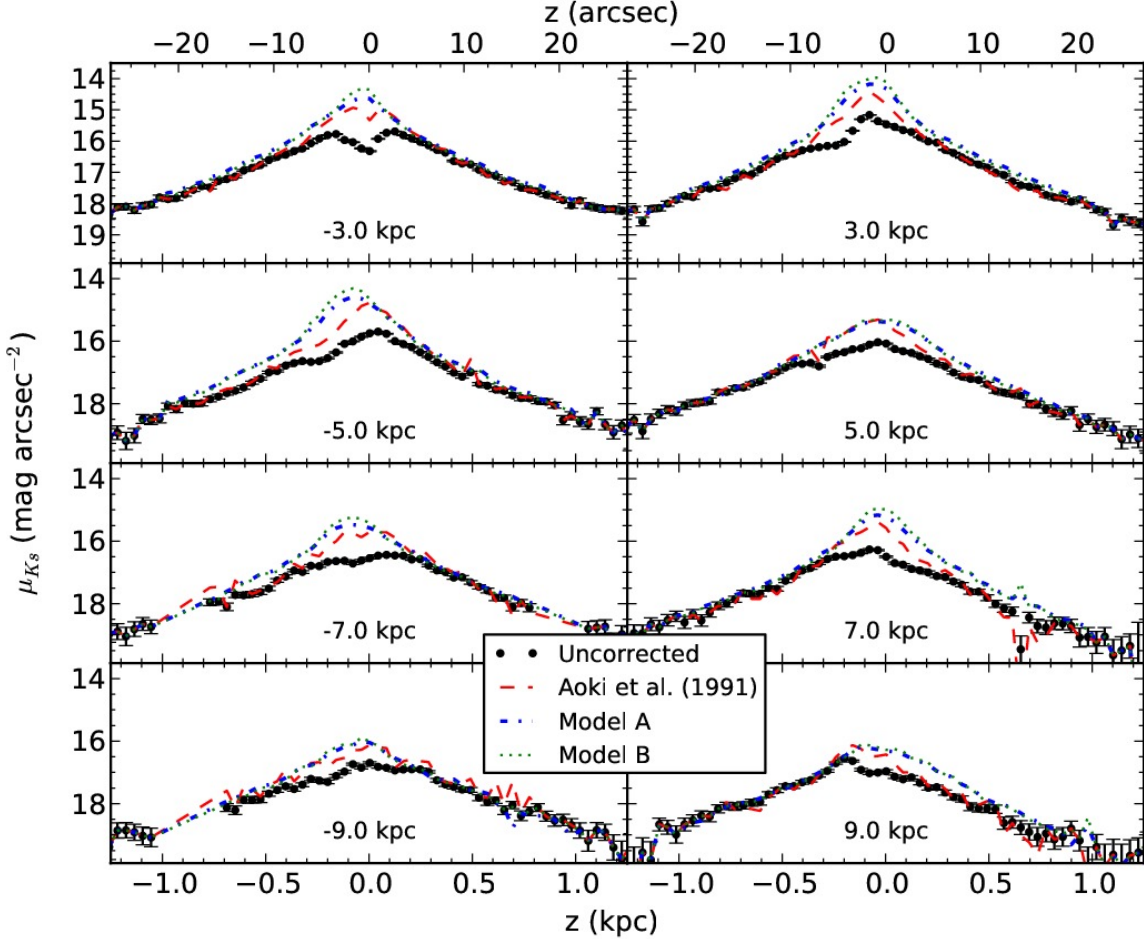


FIG. 8.— Comparison of methods for attenuation correcting K_s -band data. Black points: uncorrected data. Red dashes: our data corrected using the foreground screen model of Aoki et al. (1991). Blue dot-dashed line: data corrected using Model A. Green dotted line: data corrected using Model B. The text near the bottom of each panel shows the radius where each profile was extracted, with positive radii on the SW side. The lack of data near ~ 1 kpc on the -7 kpc vertical profile and near ~ 1 kpc on the -7 and -9 profiles is due to foreground stars.

tor. Comparing the radial profiles on both sides of the bulge shows the significant amount of stochastic structure in the midplane. In addition to the bumps noted by Aoki et al. (1991) the southwest side has another light enhancement at ~ 7.5 kpc and a marked dearth of light at ~ 5.5 kpc. The northwest side appears to have fewer of these strong features, however, although it certainly has its fair share of smaller bumps and wiggles. All of these features point to the strong observable effect of clumpy dust and starlight, even at these long wavelengths.

We compare the K_s -band major axis radial profile from Figure 10 to its dust-corrected counterpart (using Model B) in the left panel of Figure 12. The dust-corrected profile is uniformly brighter than the fiducial profile, which is to be expected. Several local surface-brightness peaks seen in the observed profile are not present in the dust-corrected profile (at $R \sim 3$ kpc, for instance, on the SW side) while others have been enhanced. The apparent star-forming regions mentioned in the previous section all correspond to local maxima in the dust-corrected profile; of particular note is point ‘B’, which does not stand out on the original profile. Also interesting is the ‘trough’ on the SW side of the dust-corrected profile between 4 and

6.5 kpc. While the original profile has a local minima in the same region, it is much smaller in radial width. It seems likely that striking appearance of this feature is due to a combination of a real intensity drop-off at $R \sim 4$ kpc and the enhancement of the underlying smooth profile at ~ 7 kpc (point ‘C’).

Just from looking at the attenuation-corrected radial surface-brightness and color profiles (Figures 11 and 12) it is difficult to discern whether the asymmetries in the flux and color profiles are due to stellar density enhancements, intrinsic color variations, or both. Figure 13 shows the magnitude and color differentials between the SW and NE sides of the major axis profiles, where ΔX is defined as the magnitude difference between corresponding ~ 40 pc² cells at the same radii but on opposite sides of NGC 891’s midplane. Figure 13 clearly indicates that asymmetries in surface brightness are correlated with color — brighter regions of NGC 891’s midplane are also bluer. The mean attenuation-corrected J- K_s and H- K_s colors for ΔJ and $\Delta H = 0$ are ~ 0.77 and ~ 0.12 mag, respectively, roughly the color of a K2III star. There are minor (~ 0.03 mag) differences in these colors between the two sides, but are well within the dispersions of the

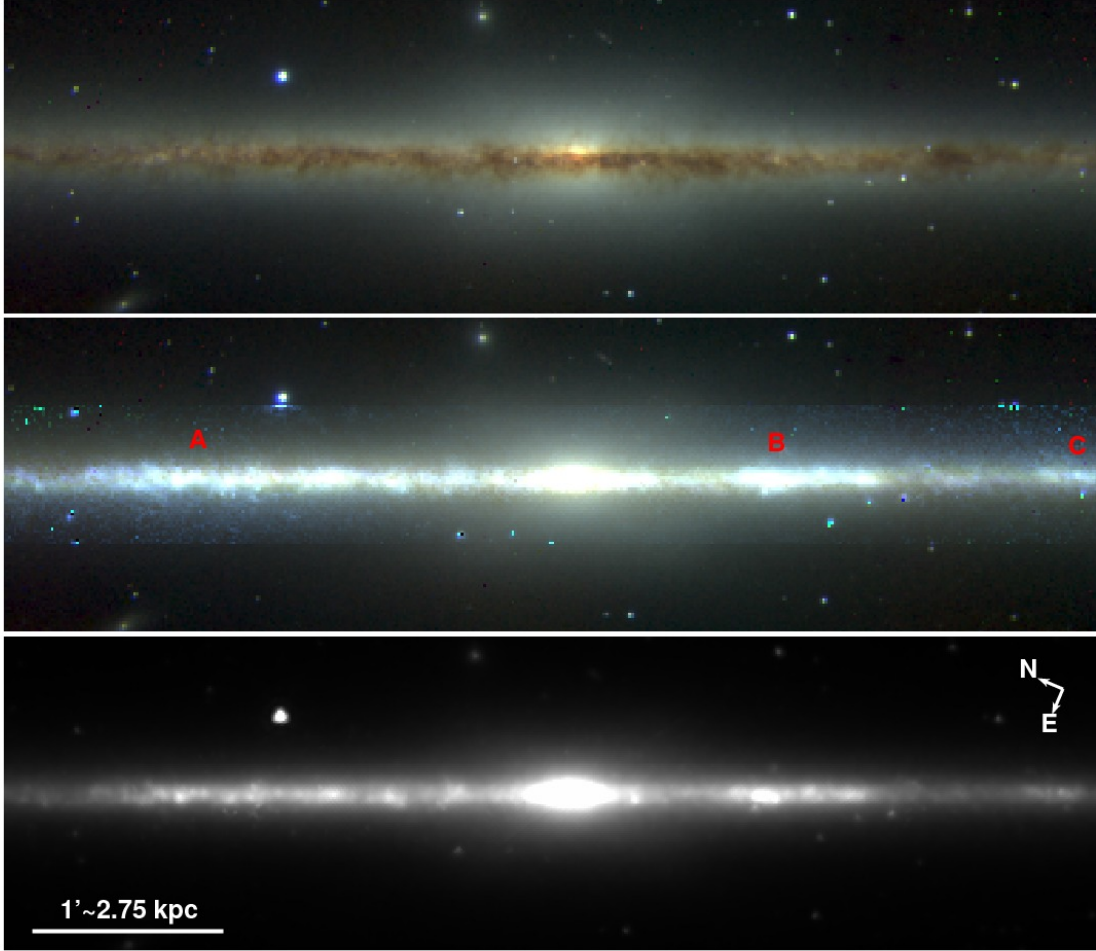


FIG. 9.— Top: central region ($5.8 \times 1.6 \sim 16 \times 4.4$ kpc) of NGC 891. Middle: central region of NGC 891 after dust correction. Bottom: IRAC $4.5\mu\text{m}$ image of the central region of NGC 891. The top two images are JHK_s color composites with the same scaling. Red labels indicate regions outside of the central bulge which appear to have excess flux over what would be expected from a smooth exponential, possibly indicating star-forming regions or spiral structure.

data.

To approximate the effect of star formation on these Δ metrics we also compute how the colors would change if the excess midplane light between the two sides of NGC 891 is due to a hot star. We find that the $\Delta\text{J}-\text{K}_s$ index is well fit by an O-type star, while the trend for $\Delta\text{H}-\text{K}_s$ vs. ΔH is underpredicted for any stellar type. A full investigation of this minor discrepancy is beyond the scope of this work, but the general trend is clear. Rather than merely being overdensities of old stars, asymmetries in the radial major-axis profile of NGC 891 are being caused by the addition of young stellar populations to the underlying stellar density. In some cases these asymmetries are likely due to individual regions of enhanced star-formation, but the broad nature of several features are at much larger scales than would be expected for localized star-forming regions. For instance, the surface brightness is relatively constant on the NE side of NGC 891 between 3 and 6 kpc, while the aforementioned SW ‘trough’ is ~ 2 kpc wide. The simplest explanation for these features is that we are viewing projected spiral structure, which NGC 891 is believed to possess (Kamphuis et al. 2007).

To verify the validity of our dust correction we compare

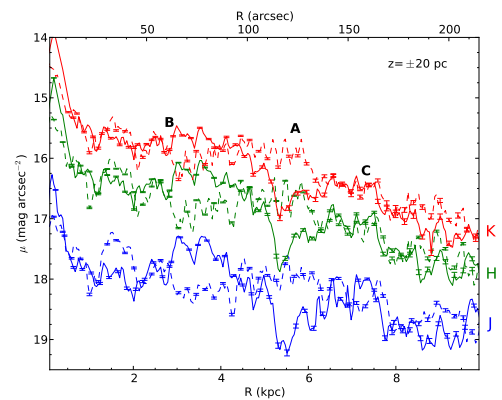


FIG. 10.— Major axis ($z=0$, vertical aperture size ~ 40 pc) radial light profiles of NGC 891 *without* dust correction. Blue, green, and red lines represent J-, H-, and K_s -band data, respectively. Solid lines show the SW side of NGC 891, while dashed lines show the NE side. Labels ‘A’, ‘B’, and ‘C’ are at the positions of the regions of interest shown in Figure 9. Error bars are not shown for every point to improve readability.

IRAC 3.6 and $4.5\mu\text{m}$ major axis profiles to the dust-

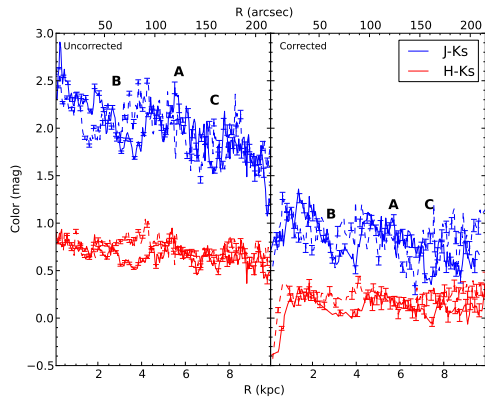


FIG. 11.— Major axis ($z = 0$, vertical aperture size ~ 40 pc) J- K_s and H- K_s radial color profiles of NGC 891. Line styles, labels, and errors are the same as for Figure 10. Left panel shows profiles without dust correction, while the right panel shows the profiles after the effects of attenuation have been removed.

corrected K_s profile in the middle and right panels of Figure 12. The IRAC data in general shows the same non-axisymmetric features as the dust-corrected K_s -band profile, with a few local exceptions (e.g. at ~ 3 and ~ 5.5 kpc on the SW side). The IRAC profiles are also globally fainter by up to $0.5 \text{ mag arcsec}^{-2}$, whereas for starlight the unattenuated $K_s\text{-}3.6/4.5\mu$ color should be zero (in our Vega photometric system) due to all filters being in the Rayleigh-Jeans regime. These discrepancies are *entirely* due to dust attenuation in the 3.6 and $4.5\mu\text{m}$ bands: we computed dust corrections for these filters in the same way as for the NIR, which when applied to the IRAC major axis profiles produces profiles virtually identical to the K_s -band data (Figure 14).

A series of K_s -band vertical profiles at several radii are shown in Figure 15. Gray points show the profiles including the effects of dust, while black points have been attenuation corrected. The midplane attenuation is roughly constant at $\sim 1.5 \text{ mag arcsec}^{-2}$ out to $R = 8.5$ kpc. The amount of attenuation quickly decreases with z , however, and by $z \sim 0.5$ kpc the effects of dust on the K_s -band vertical profiles are almost negligible. At $R \sim 9$ kpc there is a truncation in the central SB of the dust corrected profiles but not of the uncorrected ones. This scenario can only result from a cutoff in *both* the light near the midplane as well as the dust attenuation. This feature illustrates the importance of properly accounting for dust attenuation, as the uncorrected profile appears to be smoothly decaying across this threshold.

4.2. Image Fitting

4.2.1. Model Profiles

The intensity distribution of an edge-on spiral with a radially exponential disk luminosity density distribution at all heights can be described, in the absence of attenuation, by the analytic function

$$I(R, z) = I_0 \frac{|R|}{h_R} K_1 \left(\frac{|R|}{h_R} \right) f(z), \quad (3)$$

where I_0 is the central flux, K_1 is the modified Bessel function of the first order, and $f(z)$ is a function governing the vertical light distribution (van der Kruit & Searle 1981).

A simple analytic description of the vertical density profile of a spiral galaxy has been proposed by van der Kruit (1988) to be of the form:

$$f(z) = 2^{-2/n} \text{sech}^{2/n} (n|z|/(2h_z)), \quad (4)$$

where n varies between 1 and ∞ . The limiting behavior of this formula produces a sech^2 distribution

$$f(z) = \frac{\text{sech}^2(|z|/(2h_z))}{4} \quad (5)$$

when $n=1$ and the exponential distribution

$$f(z) = \exp(-|z|/h_z) \quad (6)$$

when $n = \infty$. For convenience we include the factor of 4 in the sech^2 profile with I_0 and use

$$f(z) = \text{sech}^2(|z|/(2h_z)) \quad (7)$$

instead.

The first attempts to fit the detailed vertical surface-brightness profiles of edge-on spirals began by treating the disk as a locally isothermal self-gravitating sheet (van der Kruit & Searle 1981), which results naturally in the sech^2 model (Spitzer 1942). As a result this model is generally referred to as the ‘isothermal’ distribution. Note, however, that this strict physical connection is lost when considering multiple disks, rotating disks with radial gradients, and/or disks embedded in a dark matter halo. Nonetheless, the sech^2 profile is not a bad descriptor of many observed disk vertical light profiles. More recent work has found that a steeper profile appears to fit some data better — usually an exponential profile (Wainscoat et al. 1989; Aoki et al. 1991; Xilouris et al. 1999), although sometimes the intermediate $n = 2$ ‘sech’ profile is employed (Barnaby & Thronson 1992; Rice et al. 1996). A theoretical framework which produces vertical surface-brightness distribution much closer to that of an exponential from physical conditions in spiral galaxies (by considering the gas in addition to the stars) has been developed partly in direct response to these experimental findings (Banerjee & Jog 2007). Comerón et al. (2011b) also find that the vertical density profiles for dynamically consistent models of multiple self-gravitating disks are steeper than a sech^2 function. Discussed further in Section 5.2, their models are well characterized by the intermediate sech vertical profile.

In general, however, there is currently no concrete consensus for which type of profile (or superposition of profiles) better represents the underlying distribution of stars, due largely to the fact that both the exponential and sech^2 profiles have significant deviations from each other only at small heights, exactly the place where dust obscuration is most prevalent. In this work, since we are able to accurately remove the deleterious effects of dust on the data, we will use both exponential and sech^2 profiles in our vertical fits and see if we are able to distinguish one as clearly better in a statistical sense. Additionally, since NGC 891’s thin and thick disks are well known (e.g. Morrison et al. 1997; Ibata et al. 2009) and there is a clear super-exponentiality in the dust corrected profiles near the midplane in Figures 8, 9, and 15, we expect our fits to require three separate vertical components in order to constrain the data at all z .

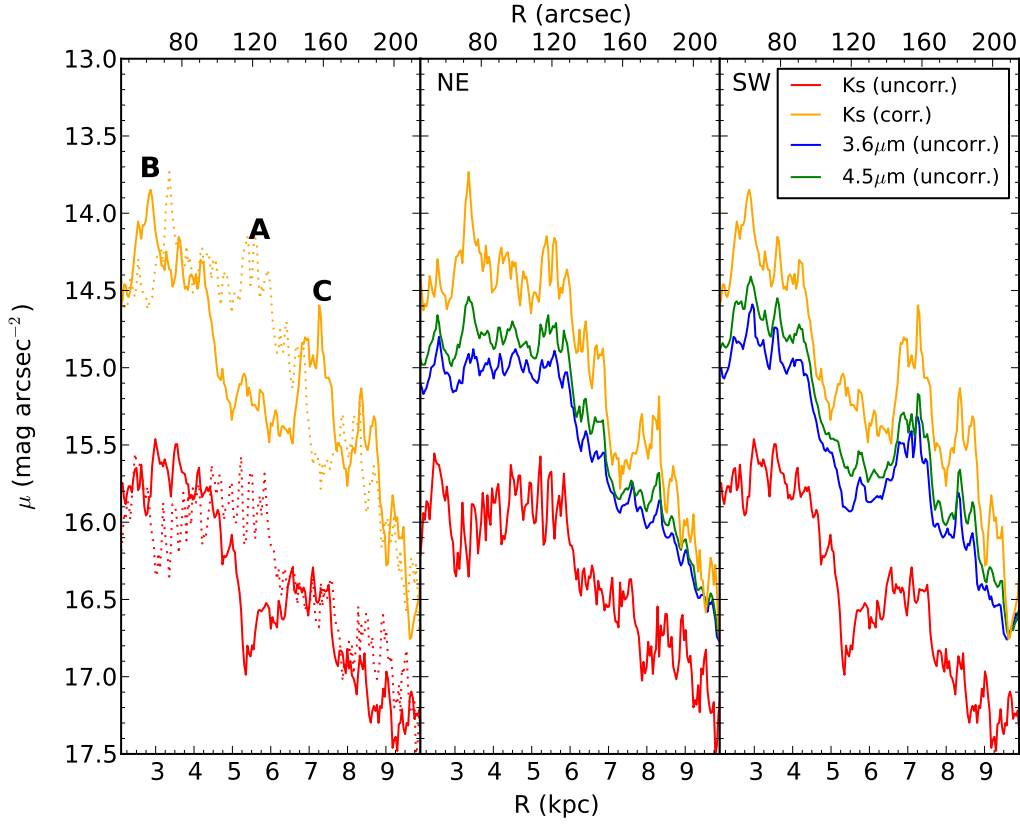


FIG. 12.— Major axis ($z = 0$, vertical aperture size ~ 40 pc) radial surface-brightness profiles. Left: comparison of profiles before (red) and after (orange) dust correction in the K_s -band. Solid lines show the SW profile, while dotted lines denote the NE side of NGC 891. Labels denote regions of interest discussed in the text. Middle (right) panels show uncorrected and corrected K_s -band major axis profiles compared to IRAC $3.6\mu\text{m}$ and $4.5\mu\text{m}$ data on the NE (SW) sides of NGC 891.

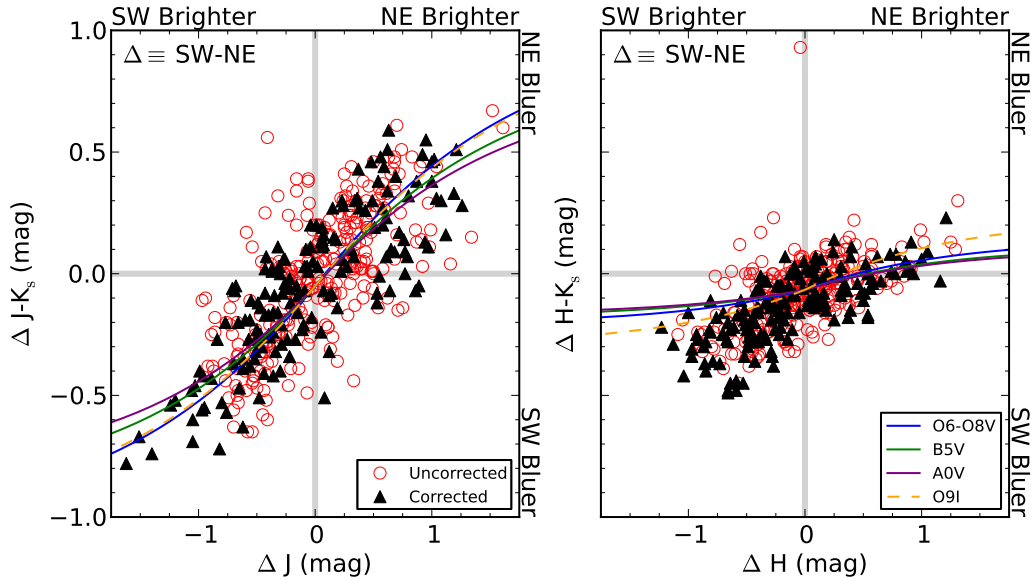


FIG. 13.— Left: $J-K_s$ color differentials between SW and NE sides of NGC 891's major axis as a function of J magnitude differentials. Right: same, but for $H-K_s$ as a function of H . Red open circles and black filled triangles denote data before and after dust correction, respectively. Lines show how the colors would change if stars of a given spectral type (from Tokunaga 2000) are added to either the SW or NE side of the galaxy. The $J-K_s$ color variance is well explained by a late O-type star, although none of the stellar templates are able to fully match the $H-K_s$ data.

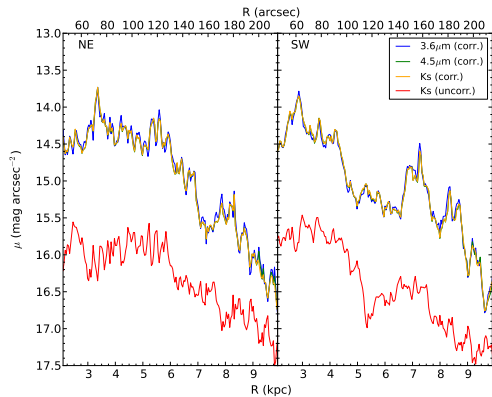


FIG. 14.— Same as the middle and right panels of Figure 12, but with attenuation corrected IRAC 3.6 and 4.5 μ m profiles.

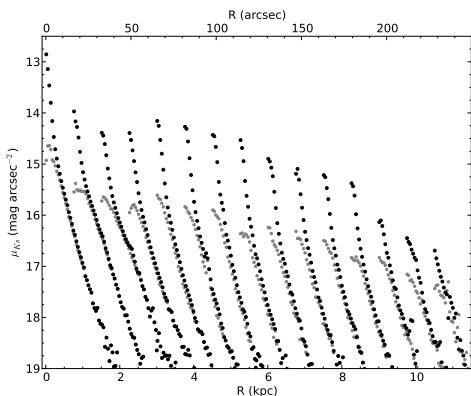


FIG. 15.— Vertical K_s-band profiles of NGC 891. All four quadrants of the galaxy have been averaged together. The leftmost point of each profile is at the radius of that profile, starting at R = 0 kpc and stepped every 0.75 kpc. Gray points are the uncorrected profiles, while the black points have been attenuation corrected. NGC 891 appears to have a roughly constant midplane attenuation of ~ 1.5 mag from just outside the very center of the galaxy to 9 kpc in radius. At radii larger than 9 kpc, both the intrinsic amount of light and dust attenuation fall off at a much steeper rate.

4.2.2. Seeing Convolution

Normally, observational studies of edge-on spirals have not required a detailed treatment of the effects of seeing on the observed profiles. This is a result of the combination of large pixel-sizes on detectors and the censoring of regions near the midplane to avoid dust effects (e.g. de Grijs & van der Kruit 1996; de Grijs et al. 1997). However, in this work the seeing correction is of significant importance, especially in distinguishing between sech^2 and exponential fits, where the seeing serves to smooth out the exponential profile and make it appear more like a sech^2 .

We make the simplifying assumption that the seeing profile can be approximated by a 2D Gaussian point-spread-function, as in Pritchet & Kline (1981). Then, the convolution is

$$I_{conv}(R, z) = \frac{1}{2\pi\sigma^2} \int_{-\infty}^{\infty} I(r', z') \exp\left(\frac{-(R-r')^2}{2\sigma^2}\right) \exp\left(\frac{-(z-z')^2}{2\sigma^2}\right) dr' dz', \quad (8)$$

where σ is the FWHM of the seeing. Since all the profiles we are considering here are of the form of equation 3 we can perform the convolution separately in R and z :

$$I_{conv}(R, z) = \frac{I_0}{2\pi\sigma^2} \int_{-\infty}^{\infty} \frac{|r'|}{h_R} K_1\left(\frac{|r'|}{h_R}\right) \exp\left(\frac{-(R-r')^2}{2\sigma^2}\right) dr' \times \int_{-\infty}^{\infty} f(z) \exp\left(\frac{-(z-z')^2}{2\sigma^2}\right) dz'. \quad (9)$$

For both exponential and sech^2 profiles we used the ‘convolve’ function in the numpy Python library. For every value to be convolved the surface-brightness profile was sampled with a spacing of 0.1 times the seeing (FWHM = $0''.9$) over a range of values equal to six times the seeing in either direction. The Gaussian kernel was sampled at the same spacing between -3 and $+3$ times the seeing. This scheme ensured that the convolution did not miss any significant amounts of flux due to edge effects from either the convolution kernel or the function, while minimizing the computation time required to perform the integral.

When the relevant scale-length or -height is much larger than the seeing, the effect of the convolution on the original profile is negligible. This is especially true at large distances from the center of the profile. Since the radial scale-length is much larger than the seeing we use the unconvolved radial intensity profile in our fitting analyses to minimize computation time.

4.2.3. 2D Fitting

With the surface-brightness profiles corrected for the attenuation and convolutions for seeing in place, we now fit the intrinsic distribution of starlight. While one-dimensional fits have been successfully employed to compare single-component surface-brightness models to data, Morrison et al. (1997) make a compelling argument, based on degeneracies between free parameters, for the necessity of fully 2D fits when multiple stellar distributions overlap. We therefore opt to model our data exclusively with image-based fits. We choose to model the K_s-band, as it is where both the dust correction and stellar population-mismatch errors will be smallest (due to the decreasing attenuation with increasing wavelength and all stellar fluxes being on the Rayleigh-Jeans tail).

Before performing our fits, however, we first mask the image based on several criteria. All pixels with flux from foreground or background contaminants are masked, as well as pixels with errors > 1 mag (while large-error pixels can still contribute to a χ^2 fit in aggregate, gains from leaving these pixels in will be minimal and removing them allows for computational speedup in the fitting process). Contaminant masking was done by hand and whenever possible we choose to be conservative. We also mask out all pixels with $R < 3$ kpc to remove any pixels dominated by “bulge” light. We refer to the bulge light in quotations because, as we shall see in Section 4.2.5, the central light distribution is complex and likely non-axisymmetric. For exactly these reasons we wish to focus first on the outer (in radius) disks.

We use the Python lmfit⁸ extension to the Levenberg-Marquardt nonlinear least-squares minimization routine

⁸ <http://newville.github.com/lmfit-py/>

in `scipy.optimize.leastsq` (which is itself based on the MINPACK-1 library). Although we report surface-brightness values in mag arcsec^{-2} , all fitting is performed on flux values to preserve error estimates. To avoid false minima, we ran the fit 100 times for 1- and 2-component models and 200 times for 3-component models. The initial guesses of all free parameters for each run were chosen randomly within upper and lower limits based on what we considered to be reasonable ranges for spiral galaxies (Table 3). The model with the lowest χ^2 was selected and used as the input guess to 100 bootstrapping iterations, finding, as Morrison et al. (1994) did, that standard error estimates from the nonlinear fit were often too small. Note that only random uncertainties are shown in Table 3; the $\lesssim 8\%$ systematic error on the central surface brightnesses from input stellar SED mismatch (Section 3.3) is not shown.

We fit models with 1-, 2-, and 3-components for both attenuation corrections, motivated by the presence of three disk components in the MW: the young, star-forming disk, the thin disk, and the thick disk (van Dokkum et al. 1994, although Bovy et al. 2012 indicate that perhaps the boundaries between the disks are not so well-defined). It is important to note that we do not force the physical parameters of the super-thin or thin disks to resemble those seen in NGC 891 and/or the MW by prior studies by way of limiting our parameter space (although we do restrict the parameter space for the thick disk; see next paragraph for details). On the contrary our externally imposed constraints are extremely permissive and allow for fitted values that can either agree or disagree with the literature.

For models with one or two components each component had three free parameters: μ_0 , h_R , and h_z . Additionally, a single vertical offset for each model was fit simultaneously, to remove the effects of any small errors from our choice of galaxy center. Because any such errors in R will be much smaller than h_R (and therefore have minimal effect on the fits) to avoid additional computational overhead we do not allow a radial offset in the fits. Therefore, for a model with 1 (2) vertical component(s), there are 4 (7) free parameters. Preliminary 3-component fits were unable to consistently select physically plausible fits due to the low S/N at large heights; however, visual inspection of the 2-component residuals showed an excess of light at large heights above the mid-plane, especially when fitting with sech^2 profiles. This arises from the shallower inner profile of the sech^2 function which drives the fits (in a χ^2 sense) to a smaller h_z . To reduce our parameter space (and therefore the degeneracies) we restrict the scale-length and -height of the 3rd (most extended) component to values given by Ibata et al. (2009), who used HST to obtain very precise scale parameters with resolved star-counts of NGC 891's thick disk. We do, however, leave the flux normalization for this component a free parameter, to allow for bandpass differences and an incomplete understanding of the integrated SED from the star-count analysis. Therefore our 3-component fits involve 8 free parameters. The results from all fits are shown in Table 3.

Generally there is very good agreement between the fits from the two attenuation correction models. The 1-component fits are nearly identical, especially for the

exponential case. The main distinction of note for the 2 and 3-component models is that the central surface-brightnesses of the innermost (super-thin) disk fits are smaller for Model A than for Model B, which is to be expected given the increased amount of attenuation correction for a given color in Model B (see Figures 7 and 8). Since none of the differences in fitted parameters between Model A and B would substantially affect our initial analysis (although the differences between the models are more relevant for our discussion of the total disk luminosities; see Section 5.1.2), for simplicity we will focus the discussion on the fits from Model B because it appears to provide a better fit to the colors of the data (c.f. Figures 4-5 and Section 3.3).

Several vertical slices of the data, overlaid with the relevant 1D portions of the fits, are shown in Figures 16-18. The single component fits (Figure 16) are clearly too simple, failing to match the peak intensity at the mid-plane as well as at high latitude. Figure 17 illustrates the dramatic improvement between the 1 and 2-component fits. Whereas the single component fit had difficulty fitting the data at any height, the 2-component sech^2 fit does a reasonable job within ± 0.5 kpc, while the exponentials appear to accurately fit almost the entire profile. The difference in reduced χ^2 between using sech^2 functions versus exponentials is relatively small compared to the statistical improvement in adding the second component to the fits, however, since the regions of largest discrepancy in the 2-component fits are where the noise is largest. This discrepancy arises because a single exponential (even with the seeing correction) is more peaked than a sech^2 and is therefore better able to fit the (most statistically relevant) midplane regions, leaving the second exponential to fit the outer regions.

While adding a third component decreases the reduced χ^2 of the exponential fits only by a small amount, the improvement in the sech^2 fits is more significant, both in the χ^2 sense and upon visual inspection of Figure 18. The 3-component exponential and sech^2 fits are virtually indistinguishable from each other, both in a visual and statistical sense, and both are clearly able to fit the vertical profile at all heights. A representative plot of vertical surface brightness fits with the contributions of the individual disks is shown in Figure 19. First, the visual improvement resulting from adding the third component is clearly noticeable, especially at heights above ~ 0.75 kpc. Additionally, while the total surface-brightness profiles of the 3-component exponential and sech^2 fits are very similar, there are noticeable differences in the form of the individual components. These differences are largest in the relative μ_0 between the exponentials and the sech^2 s, mostly to compensate for the flatter central profile of the sech^2 profiles.

Even with the 3-component models, we find reduced $\chi^2 > 1$. This could be due to an underestimation of our errors, most likely in the attenuation correction. However, given the relative simplicity of our model compared to the complex nature of a galactic system (e.g. the model is perfectly axisymmetric), the fact that we do not recover a reduced $\chi^2 \sim 1$ is not surprising. Our 2D fits do not take into account the potential effect of warps, star-forming regions, spiral arms, or any other non-axisymmetric structure. Despite these limitations,

TABLE 3
TWO-DIMENSIONAL FITS

Parameter ^a	Allowed Range		One Disk				Two Disks			
	Min	Max	exp	Δ^b	sech ²	Δ^b	exp	Δ^b	sech ²	Δ^b
$\mu_{0,1}$	25	10	14.00±0.018	0.04	14.52±0.020	0.13	13.26±0.040	-0.58	13.53±0.026	-0.66
$h_{R,1}$	0.1	10	3.55±0.027	0.12	3.67±0.025	0.11	2.42±0.045	-0.89	2.54±0.032	-0.70
$h_{z,1}$	0.01	2.5	0.28±0.002	0.00	0.19±0.002	0.01	0.12±0.004	-0.10	0.07±0.001	-0.02
$L_{tot,1}^c$	1.37×10 ¹¹ (100)	...	1.19×10 ¹¹ (100)	...	7.92×10 ¹⁰ (47)	...	7.57×10 ¹⁰ (48)	...
$\mu_{0,2}$	25	10	15.29±0.101	-1.91	15.68±0.067	0.07
$h_{R,2}$	0.1	10	4.44±0.241	0.63	4.30±0.178	0.89
$h_{z,2}$	0.01	2.5	0.48±0.016	-0.77	0.33±0.007	-0.02
$L_{tot,2}^c$	8.97×10 ¹⁰ (53)	...	8.33×10 ¹⁰ (52)	...
Δz	-0.1	0.1	0.05±0.001	0.00	0.05±0.001	0.00	0.05±0.001	0.00	0.05±0.001	0.00
Reduced χ^2	7.32	1.09	11.7	1.70	4.21	-0.19	4.61	-0.5

^a μ values in mag arcsec⁻¹, h_R , h_z , and Δz values in kpc.

^b Reported values in ‘exp’ and ‘sech2’ columns are for Model B, and Δ = Parameter_{Model B} - Parameter_{Model A}.

^c Total luminosities are given in solar units where $L_{\odot,K} = 3.909 \times 10^{11} \text{WHz}^{-1}$ (from Binney & Merrifield 1998). Values in parenthesis are the percentage of the total disk luminosity in that component.

^d Fixed values from Ibata et al. (2009).

TABLE 3
TWO-DIMENSIONAL FITS, CONTINUED

Parameter ^a	Allowed Range		Three Disks			
	Min	Max	exp	Δ^b	sech ²	Δ^b
$\mu_{0,1}$	25	10	13.08±0.040	-0.94	13.41±0.023	-0.67
$h_{R,1}$	0.1	10	1.96±0.038	0.13	2.32±0.022	-0.37
$h_{z,1}$	0.01	2.5	0.08±0.004	0.02	0.06±0.001	0.00
$L_{tot,1}^c$	5.05×10 ¹⁰ (29)	...	6.62×10 ¹⁰ (38)	...
$\mu_{0,2}$	25	10	14.52±0.096	0.47	15.32±0.067	0.35
$h_{R,2}$	0.1	10	3.87±0.118	0.46	4.11±0.114	0.51
$h_{z,2}$	0.01	2.5	0.29±0.010	0.04	0.25±0.006	0.03
$L_{tot,2}^c$	9.60×10 ¹⁰ (55)	...	8.41×10 ¹⁰ (48)	...
$\mu_{0,3}$	25	10	17.81±0.015	0.04	18.70±0.015	0.05
$h_{R,3}$	4.80 ^d	...	4.80 ^d	...
$h_{z,3}$	1.44 ^d	...	1.44 ^d	...
$L_{tot,3}^c$	2.85×10 ¹⁰ (16)	...	2.52×10 ¹⁰ (14)	...
Δz	-0.1	0.1	0.05±0.001	0.00	0.05±0.001	0.00
Reduced χ^2	3.77	-0.47	3.65	-0.55

however, the reduced χ^2 is still effective at distinguishing between the relative goodness-of-fit of models, as shown by the improvement from 1-component fits to 3-component fits both in reduced χ^2 and upon visual inspection.

4.2.4. Disk Asymmetries

To investigate the impact of non-axisymmetric structures on our model fits to NGC 891, we constructed model - (dust-corrected) data residual surface-brightness images for both 3-component models (top two panels of Figure 20). These images have been masked (bad values set to zero) in the same way as for the 2D fitting (except for the inner 3 kpc, the boundaries of which are marked by dashed lines but not masked out), and smoothed by a $\sigma=2''7$ Gaussian to bring out larger-scale detail. Additionally, the K_s-band bulge determined by Xilouris et al. (1999) has been added to the model image before producing the residual. White contours show the boundaries of regions with errors <0.2 and <0.5 mag pixel⁻¹ (unsmoothed) — while we fit all points with errors <1 mag pixel⁻¹, we weight each pixel by its error and as a result the fit is most sensitive to pixels with small uncertainties.

Therefore we focus our analysis of the quality of the fit on the regions of the image with smaller uncertainties.

Several asymmetries are clearly present in Figure 20. Based on a visual inspection of the data before resampling, at least three of them (labeled in Figure 20 and also shown in Figures 1 and 9) are likely to be regions of enhanced local star formation in NGC 891. Oosterloo et al. (2007) find a mild HI warp in NGC 891 (position angle = 1.5°). There are some slight indications of this warp in the data, chiefly in the excess of light over the model above the midplane at radii larger than region ‘C’ on the SW side. On extremely close inspection of the non-dust-corrected mosaics (see Figure 1, although it is difficult to distinguish in that image stretch) it is also possible to discern a similar offset in the dust, but due to the clumpiness of the dust and the faintness of this feature we are unable to make a stronger claim about whether or not it is real.

4.2.5. Fitting the Central Region of NGC 891

Beyond the specific asymmetries called out above, it is clear that these models do a poor job of fitting NGC 891’s K_s-band light within 3 kpc. In addition to the large

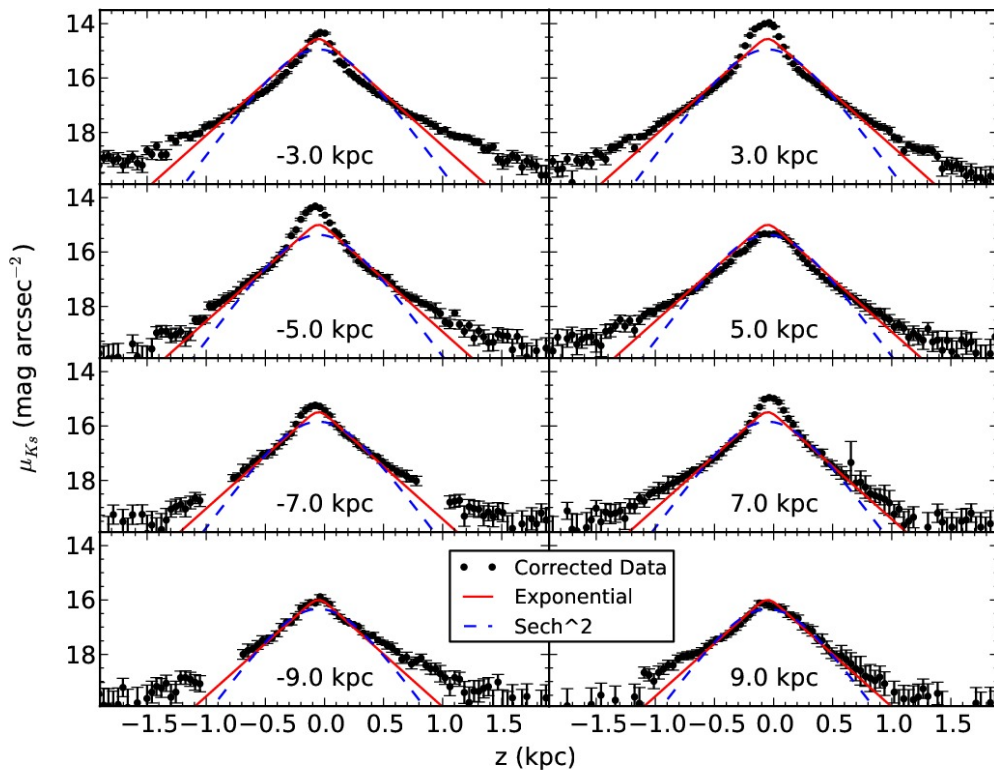


FIG. 16.— 1D vertical slices of both the K_s -band dust-corrected data (Model B) and the 2D fit for a single disk component. Data and models are shown at four radial locations on both halves of NGC 891, with radial bins of ~ 40 pc. Data are shown as black points, fits are denoted by red solid (exponential) and blue dashed (sech^2) lines. Positive radii are on the SW side of NGC 891.

amount of light above and below the midplane from the galaxy’s bar that is not reproduced in our model there is also clearly excess light in NGC 891’s nucleus — even with the addition of the Xilouris et al. (1999) bulge to the model. In contrast, just outside of the nucleus the model greatly overpredicts the flux near the midplane. The simplest explanation for this feature is that at $R \sim 3$ kpc there is a transition between disk and bar dominated regions, such that the 3-component disk is truncated within this radius and the bar does not extend beyond this radius. There is ample evidence for such truncations in other galaxies (e.g. Anderson et al. 2004). To the extent that bars arise from dynamical instabilities in the inner disk, then this is not a truncation *per se*, but a redistribution of the disk from an axisymmetric, dynamically cold stellar mass distribution to a dynamically hotter distribution with more structure.

This transition is more apparent as a function of radius in vertical profiles (Figure 21). While the 3-component model well fits the data outside of 3 kpc, the data clearly has a dearth of flux inside of 3 kpc right up until the very central regions of the galaxy. At small radii, however, there is a clear excess of flux at larger heights. We suggest this excess is due to a bar because previous studies have found evidence for such a feature in NGC 891 (e.g. Garcia-Burillo & Guélin 1995). Further, there are clearly kinks in the vertical light profile (most evident at $R=1.5$ and $z=0.8$ kpc) caused by the ‘X’ shape of the projected bar (Combes & Sanders 1981; Mihos et al. 1995;

Bureau & Freeman 1999; Bureau et al. 2006). Other than these small kinks, however, the bar appears to be very close to having a pure exponential vertical light distribution.

Understanding the galaxy’s behavior near the center is critical to estimating the total luminosity of each disk component and to fully characterize their radial distribution. Therefore we perform a second set of 2D fits on the data attenuation-corrected by Model B. While using the same basic scheme as in Section 4.2.3, this time we leave the central region of NGC 891 unblacked. This necessitates several new model parameters. We approximate the bar in edge-on projection as an outer-truncated disk. This appears to be a good approximation to the light distribution of the bar seen edge-on, and the functional form of a truncated disk simplifies our fitting procedure. Our bar model therefore has three free parameters: a central SB ($\mu_{0,bar}$), scale-length ($h_{R,bar}$), and scale-height ($h_{z,bar}$).

Since there is an excess of light at small R and z that appears morphologically disconnected from the bar emission (see the top two panels of Figure 20), it is necessary to introduce an additional component. We first attempted to fit a classical $R^{1/4}$ -law bulge to NGC 891, but found that this form made for extremely poor fits. We found instead that the central component of NGC 891 was well-fit by a nuclear disk with the same scale-height as the super-thin disk. We therefore fixed the scale-height of this component $h_{z,nuc} = h_{z,ST}$ and allowed

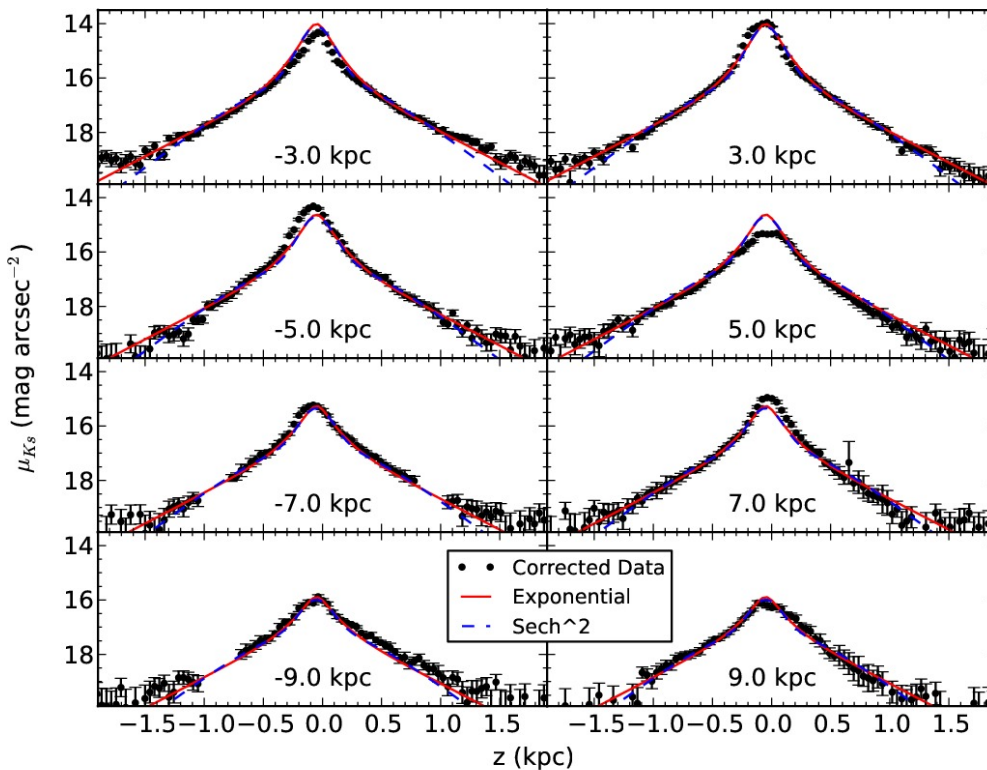


FIG. 17.— Same as Figure 16, but for two disk components.

the central SB $\mu_{0,nuc}$ and scale-length $h_{R,nuc}$ to vary.

Finally, we add a truncation radius R_{trunc} , which functions as an inner cutoff for all three main disks and an outer cutoff for the bar and nuclear disk. For simplicity this truncation is abrupt: at all points inside (outside) of R_{trunc} the main disks (bar and nuclear disk) have zero flux. In reality there will be a transition length instead of a discontinuous truncation, but we do not find that the data warrants this complication in the model. The scale-heights of the three main disks should be well determined by our original fitting scheme, and tests indicated that there were minimal changes in central SBs and scale-lengths of the thin and thick disks when the central region of NGC 891 was uncensored. Therefore we fixed the parameters of the thin and thick components at their best-fitting values in Table 3, but we allowed $\mu_{0,ST}$ and $h_{R,ST}$ to vary. We perform these new fits only for sech² disks.

The parameters of the best-fitting model are listed in Table 4 and compared to the data and untruncated 3-component sech² disk model (from Table 3) in Figure 21. The residual image from this model is shown in the bottom panel of Figure 20. The outstanding residuals that remain are associated with the ‘X’ shape pattern attributed to the bar. It would be very useful to have a simple analytic parameterization of this light distribution, but we are not aware of one in the literature. While still not perfect, adding a disk truncation, a simple representation for the bar, and a nuclear disk dramatically improves our ability to fit the inner portion of NGC 891.

The central SB and scale-length of the super-thin disk change minimally from the original fits. The bar has a scale-height ~ 1.5 times that of the thin disk, but substantially smaller than the thick disk, which agrees with a visual inspection of our images. The reduced χ^2 of this fit is somewhat larger than for the fits with only the three disk components; this is due to the unmodeled ‘X’ shape bar pattern.

5. DISCUSSION

5.1. Literature Comparisons

5.1.1. Radial and vertical Disk Scale-lengths

Several groups have estimated NGC 891’s thin disk parameters. Studies simultaneously fitting the thin and thick disk components of NGC 891 typically find optical thin disk scale-heights of ~ 0.5 kpc (Ibata et al. 2009; Morrison et al. 1997 and references therein). Using single component exponential fits in the infrared, Aoki et al. (1991) determine a K-band scale-height of 0.35 kpc, while Xilouris et al. (1999) find a K-band scale-height of 0.34 kpc and a K-band scale-length of 3.87 kpc with their single-disk model. Due to the resolution and depth of these studies these single-disk fits probe the region of the surface-brightness profiles where the thin disk dominates, and thus are most directly matched to this component when compared to multi-component fits. The decrease in scale-height in the NIR may be due to the decreased role of dust attenuation. If vertical profiles are fit to data that hasn’t been corrected for attenuation the dust will function to artificially increase the inferred scale-heights.

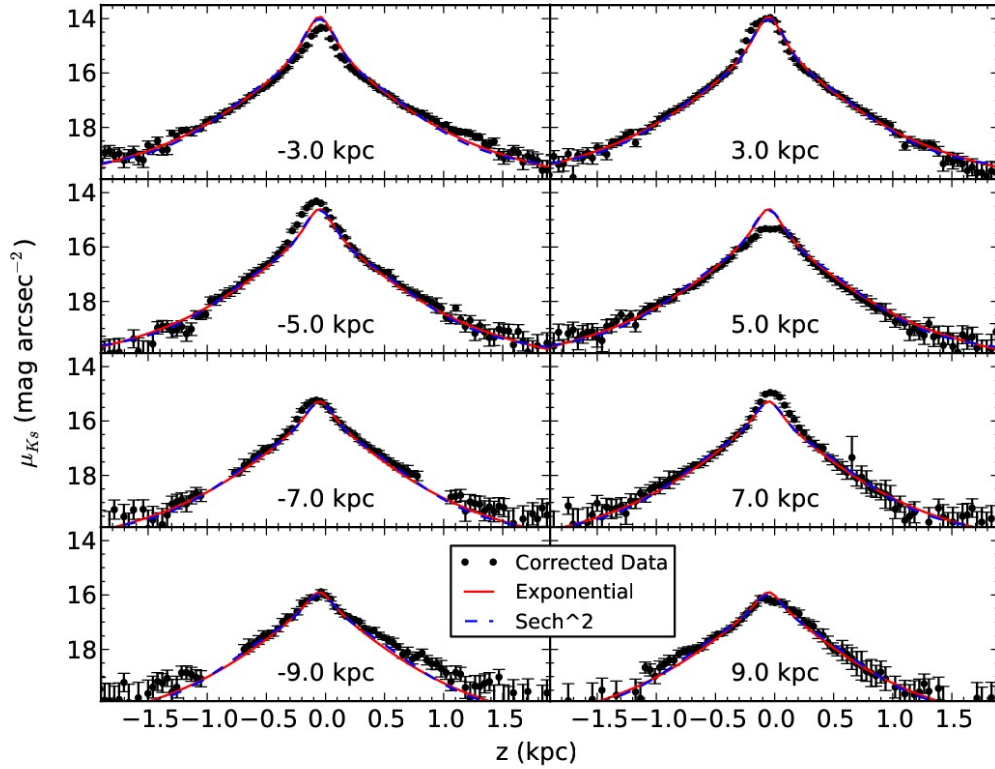


FIG. 18.— Same as Figure 16, but for three disk components.

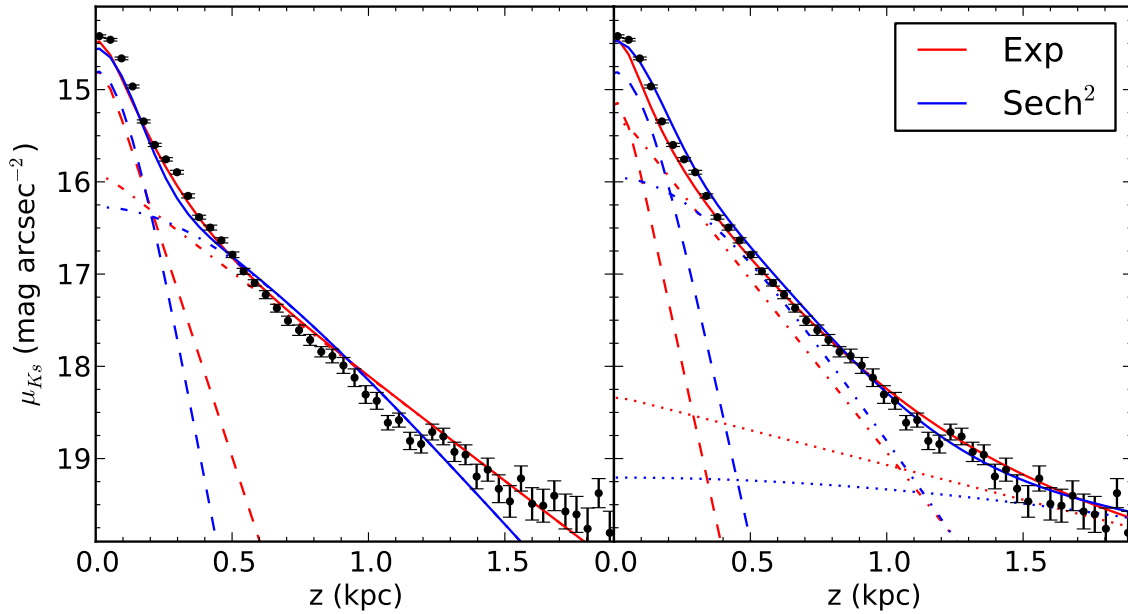


FIG. 19.— Representative vertical profile for NGC 891 ($R=4.5\pm 0.04$ kpc), overlaid with the best-fitting two-component (left) and three-component (right) seeing-convolved exponential (red) and sech^2 (blue) models. Black points are data (averaged over all four quadrants of the galaxy), while solid lines show the total surface-brightness profiles of the models. The surface-brightness profiles of the individual disks which make up the models are denoted by dashed, dot-dashed, and dotted lines (showing the disks in order of smallest to largest h_z). The data have been averaged over all four quadrants of the galaxy.

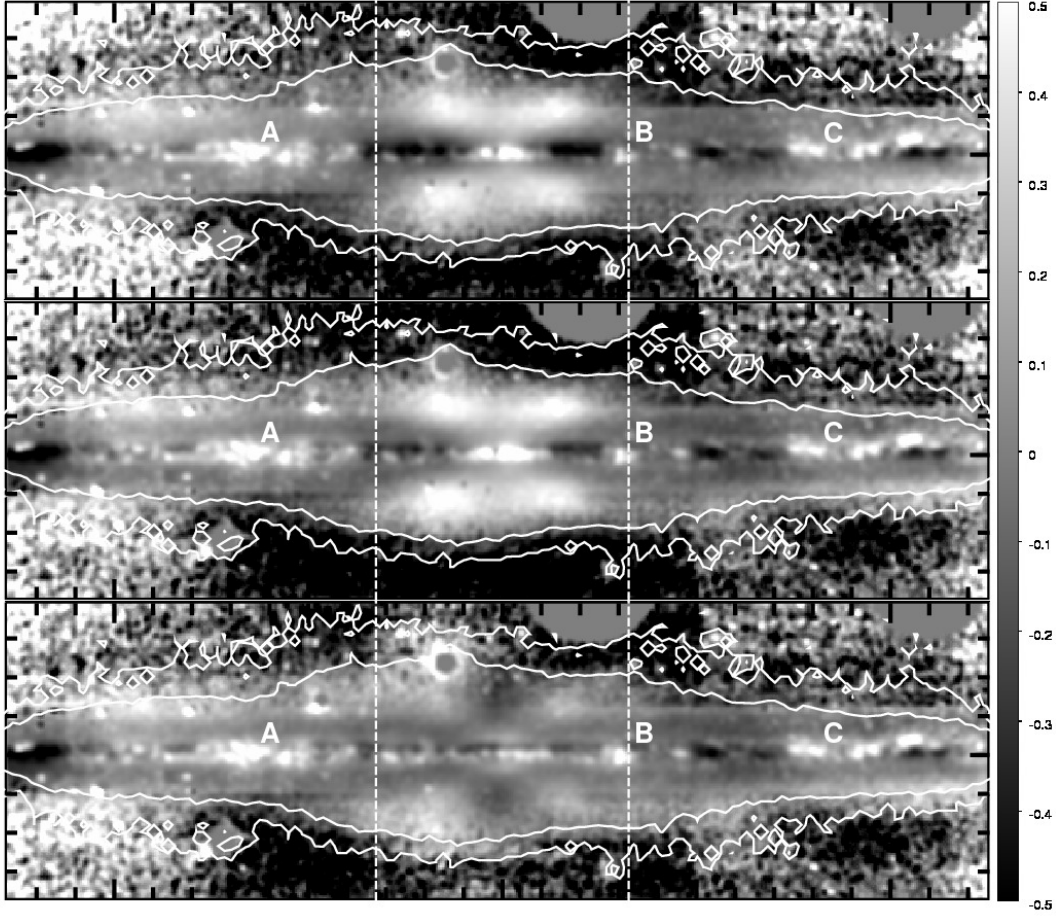


FIG. 20.— Top two panels: Residual surface brightness image (model - dust-corrected data) for the 3-component models in Table 3 (Model B attenuation correction). Top: model with exponential vertical light distribution. Middle: model with sech^2 vertical light distribution. The bottom plot shows the residual image for the model which adds a nuclear disk, bar, and bar/disk truncation to the 3-component model (Table 4). The data have been masked as they are in the 2D fitting algorithm (except for the inner 3 kpc region, not masked here, which is simply denoted by dashed lines), and smoothed by a Gaussian with $\sigma=2''.7$. Colorbar units are mag arcsec^{-2} . White contours denote 0.2 and $0.5 \text{ mag pixel}^{-1}$ errors in the unsmoothed data. White labels denote regions corresponding to areas which, based on a visual inspection of the images, appear to contain embedded star clusters. The full image extent is (width x height) $23.8 \times 9.6 \text{ kpc}$, where $1' \sim 2.75 \text{ kpc}$. Each tick corresponds to $20''$. The vertical dashed lines show the inner limits of the data used in the model fitting for the 3-component models. The SW side is on the right.

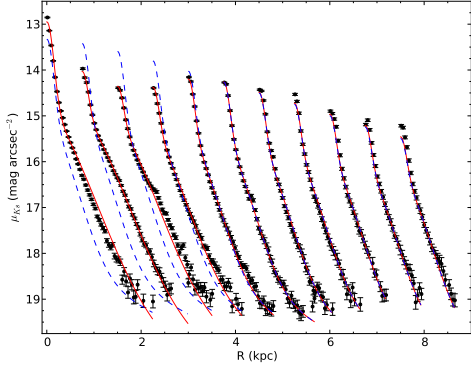


FIG. 21.— Vertical surface brightness profiles of the attenuation corrected K_s -band data (black points). All four quadrants of the galaxy have been averaged together. The leftmost point of each profile is at the radius of that profile, starting at $R = 0$ kpc and stepped every 0.75 kpc. Blue dashed lines show the best-fitting sech^2 3-component disk model without any bulge/bar components, while solid red lines show the best-fitting sech^2 3-component model with a truncation, a bar (approximated by a disk), and a nuclear super-thin disk.

TABLE 4
TWO-DIMENSIONAL SECH^2 FITS, WITH BAR AND NUCLEAR DISK

Parameter ^a	Allowed Range		sech^2
	Min	Max	
$\mu_{0,ST}$	25	10	13.39 ± 0.02
$h_{R,ST}$	0.1	10	2.30 ± 0.023
$h_{z,ST}^b$	0.06
$L_{tot,ST}^c$	4.04×10^{10} (25)
$\mu_{0,T}^b$	15.32
$h_{R,T}^b$	4.11
$h_{z,T}^b$	0.25
$L_{tot,T}^c$	6.86×10^{10} (42)
$\mu_{0,Th}^b$	18.71
$h_{R,Th}^b$	4.80
$h_{z,Th}^b$	1.44
$L_{tot,Th}^c$	2.13×10^{10} (13)
$\mu_{0,bar}$	25	10	15.42 ± 0.01
$h_{R,bar}$	0.1	10	1.28 ± 0.009
$h_{z,bar}$	0.01	2.5	0.38 ± 0.001
$L_{tot,bar}^c$	2.49×10^{10} (15)
$\mu_{0,nuc}$	25	10	13.23 ± 0.04
$h_{R,nuc}$	0.1	10	0.25 ± 0.007
$h_{z,nuc}^b$	0.06
$L_{tot,nuc}^c$	8.32×10^9 (5)
R_{trunc}	1.5	4.5	3.09 ± 0.014
Δz^b	0.05
Reduced χ^2	4.55

^a μ values in mag arcsec^{-1} , h_R , h_z , Δz , and R_{trunc} values in kpc.

^b Values fixed using best-fitting values for the 3-component sech^2 model.

^c Total luminosities are in units of $L_{\odot,K} = 3.909 \times 10^{11} WHz^{-1}$ (from Binney & Merrifield 1998). Values in parenthesis are the percentage of the total disk luminosity in that component.

Alternatively, if vertical profile fits are restricted to sufficiently large z to avoid dust, then the fit is biased toward the light distribution of the thick(er) disk components. Supporting this hypothesis is the fact that Xilouris et al. (1999) find an optical scale-height of ~ 0.4 kpc from their RT models, closer to their NIR scale-heights than the ~ 0.5 kpc found in Ibata et al. (2009) and Morrison et al. (1997).

For our single component exponential fits (the most directly comparable fits to most of the above-mentioned literature) we obtain slightly smaller scale parameters (82% smaller scale-height, 92% smaller scale-length) than Xilouris et al. (1999). Our increased resolution, combined with the fact that the super-thin part of the vertical light distribution is at high S/N, are the likely reasons for the decrease in scale-height of our single component fits. The scale-length of the model with the sech^2 vertical profile is very similar to the fit using the exponential distribution. This is unsurprising since regardless of the functional form of the scale-height we use exponentials for the scale-length. The scale-height of the sech^2 model, however, is only 68% of the exponential scale-height. Indeed, a comparison between the exponential and sech^2 scale-heights for all our models shows that the sech^2 scale-height is always somewhat smaller than the exponential scale-height. As noted above, this discrepancy arises naturally from the shallower nature of the sech^2 profile near the midplane, which forces smaller scale-heights to be used to reproduce the steeper features near the midplane.

For our multiple component fits, the thin disk is most closely approximated by the second disk component, so we will refer to it as the ‘thin disk component’. In our 2-component fits, the thin disk component has (except for the sech^2 scale-height) larger scale parameter values than the Xilouris K-band fits. This discrepancy seems likely to be due to the need for the thin disk component to fit light from both the thin disk as well as the thick disk (due to the depth of our observations), while the light nearest to the midplane is fit well by the inner disk component. Corroborating evidence for this hypothesis comes from the 3-component fits, which have thin disk component scale parameters very close to the K-band values reported by Xilouris et al. (1999).

In addition to the changing scale-heights for each disk of our 3-component models, we also see a positive correlation in the scale-lengths of the components. The scale-length of the super-thin disk for both the exponential and sech^2 fit is $\sim 50\%$ of the scale-length of the thin disk, while the thin disk scale-length is only $\sim 80\%$ of the size of the thick disk. The scale-heights, however, still change more rapidly than the scale-lengths. Defining $q \equiv h_R/h_z$, $q_{Th} \sim 3 < q_T \sim 15 < q_{ST} \sim 30$.

Of special interest in our 2- and 3-component models is the need for a disk with a scale height even smaller than that of the thin disk component of NGC 891. This component, which we term the ‘super-thin disk component,’ is usually hidden from view by the dust lane as it has a scale-height of around 60-80 pc (perhaps slightly higher, based on the results of the 2-component fits). Even prior studies which attempted dust correction/modeling could not be expected to reveal this disk in the NIR as it is very close to even our own resolution limit (~ 40 pc), and

certainly would be unresolved in the data used by e.g. Aoki et al. 1991. We note, however, that Xilouris et al. (1998) do require a super-thin disk to fit excess light in their *optical* bandpasses (which have better resolution), with $h_z=0.15$ kpc but an infinite scale-length with an arbitrary cutoff. With our data we are able to fit a non-infinite scale length, which we find to be ~ 2 kpc (again, slightly higher in the 2-component fits). This is roughly half the size of the scale-lengths of the thin and thick disk components, indicating that the stars in the super-thin disk are very centrally concentrated compared to the stars in the other disks.

A likely conjecture is that the super-thin disk in NGC 891 corresponds to the young star-forming disk seen in the MW. The average scale-heights given by Bahcall & Soneira (1980) for young (~ 90 pc) and old (~ 325 pc) stars in the MW correlate well with the best-fitting parameters for NGC 891's super-thin and thin disk components. Before now this disk has never been observed as a discrete vertical component in a galaxy similar to the MW due to dust obscuration. However the presence of a super-thin star-forming disk has been inferred from the inability of RT models to reproduce the FIR SED of edge-on galaxies based only on known thin and thick disk parameters (Popescu et al. 2000; Bianchi 2008; MacLachlan et al. 2011; Holwerda et al. 2012). In these models, the scale-height of such a disk is generally assumed to either be similar to that of the MW (e.g. Popescu et al. 2000) or the same as the dust (e.g. Bianchi 2008). Our unambiguous determination of the super-thin disk scale-height removes the need to make such assumptions. Our finding that the super-thin disk scale-length is significantly smaller than the thin or thick disk scale-length is also important since previous studies have incorrectly assumed the super-thin disk has the same scale-length as the thin disk.

5.1.2. Disk Luminosities

For our single component fits (as well as for the thin disk component of our 3-component exponential fits) we compute comparable scale-lengths and scale-heights but ~ 1 mag arcsec $^{-2}$ brighter central surface brightnesses than found by Xilouris et al. (1999). This result implies that our single component models predict $\sim 50\%$ higher total K $_s$ -band luminosities for NGC 891. Our images do go deeper than those of Xilouris et al. (1999), which would boost the luminosity of our model. Our attenuation correction, which takes into account the effects of clumpy dust, may also contribute to this discrepancy. We note that our total luminosities are in much better agreement with more recent works (e.g. Popescu et al. 2011), which will be discussed in more detail later in this section.

For exponential and sech 2 disks the total flux can be computed by integrating over R and z. Including the effect of an inner disk truncation gives

$$F_{tot,exp} = 2\pi h_z f_{\nu,0} 10^{-\mu_0/2.5} e^{-R_{trunc}/h_R} \times (h_R + R_{trunc}) \quad (10)$$

$$F_{tot,sech^2} = 4\pi h_z f_{\nu,0} 10^{-\mu_0/2.5} e^{-R_{trunc}/h_R} \times (h_R + R_{trunc}) \quad (11)$$

for the super-thin, thin, and thick disks, where R_{trunc}

is the truncation radius and $f_{\nu,0}$ is the flux zero-point. In this work we use the 2MASS value of 667 Jy for the K $_s$ -band zero-point (Cohen et al. 2003). The equations for the total flux of the bar and nuclear disk are similar:

$$F_{tot,exp} = 2\pi h_z f_{\nu,0} 10^{-\mu_0/2.5} (h_R - e^{-R_{trunc}/h_R} \times (h_R + R_{trunc})) \quad (12)$$

$$F_{tot,sech^2} = 4\pi h_z f_{\nu,0} 10^{-\mu_0/2.5} (h_R - e^{-R_{trunc}/h_R} \times (h_R + R_{trunc})). \quad (13)$$

We show the total luminosities of each component for both 3-component models as well as the model which adds a bar and nuclear disk (the ‘truncated’ model) in Tables 3 and 4.

For the truncated model we find that the bar contributes roughly the same total luminosity as the thick disk, despite being confined to the central regions of NGC 891. The nuclear disk is by far the faintest, with a total luminosity only 40% of the second least-luminous component (the thick disk). The total K $_s$ -band luminosity of the truncated model is slightly ($\sim 5\%$) smaller than the 3-component model. The fact that the K $_s$ -band light lost by truncating the disks of the 3-component model is almost entirely made up for by the light from the bar and nuclear disk is tantalizing evidence that disk instabilities have merely rearranged the orbits of existing stars in NGC 891's inner regions (e.g., Combes & Sanders 1981; Combes et al. 1990; Raha et al. 1991).

The super-thin disk has a total K $_s$ -band luminosity of 5.05×10^{10} (6.62×10^{10}) $L_{\odot,K}$ for the exponential (sech 2) three disk model. The truncated super-thin disk has a total luminosity $\sim 62\%$ of its non-truncated counterpart. Assuming the nuclear disk is an inner continuation of the super-thin disk and adding its luminosity to that of the truncated super-thin disk increases this ratio to $\sim 74\%$. Assuming that the ‘young’ stellar populations used as inputs to RT models correspond exactly to our super-thin disk, the truncated disk luminosity is about an order of magnitude larger than $5.36 \times 10^9 L_{\odot,K}$, the value assumed by Popescu et al. (2011) for modeling the integrated SED of NGC 891, and roughly 4 times larger than assumed for our RT modeling. We again note that due to the nature of our attenuation correction Model B tends to have more luminous central surface-brightnesses, but even the truncated total super-thin disk luminosity of the Model A fits are still $\gtrsim 2$ times as large than the luminosity used in Popescu et al. (2011). These discrepancies are all significantly larger than either our random or systematic errors, which are of order $\sim 10\%$.

However, when the *total* flux (bulge, young disk, and old disk) from the model used by Popescu et al. (2011) is compared to the total flux of our truncated model, they agree to within 10%. It therefore seems likely that the input SEDs used by Popescu et al. (2011) need to be adjusted, with the young stellar SED getting boosted in the NIR at the expense of flux from the old stellar SED. Adjusting the bolometric luminosities of the two components will not solve this problem — boosting the luminosity of the young component at all wavelengths will cause an over-prediction of the UV flux (or an over-prediction of the FIR light if the extra UV emission is suppressed by dust). It is plausible that Popescu et al. (2011)'s young stellar SED underestimates the impact of cool,

evolved stars, especially thermally-pulsating asymptotic giant branch stars which are known to be difficult to model and are very bright in the NIR (Maraston 2005). If this is the case it would explain why Popescu et al. (2011) are able to fit the UV and FIR flux of NGC 891 while under-predicting the NIR flux of the young stellar disk component of the galaxy. Depending on the spectral type of these cool stars the peak of the old component’s SED will shift, but it is not possible with our current data to predict exactly how these input SEDs will change.

King et al. (1990) report a B-band thin disk integrated luminosity of $6.7 \times 10^9 L_{\odot}$, which (even though it’s in the optical) should be minimally affected by dust because it is computed away from the midplane of NGC 891. Using our fitted thin-disk K_s -band integrated luminosity, the thin disk has a B- K_s color of ~ 4.5 mag (Vega), similar to a K4III (Johnson 1966) star. Using the values from what Popescu et al. (2011) call the old disk, which is most similar to our thin disk, gives a B- K_s color of ~ 5.2 mag, close to a K5III or M0III. Based on a galactic evolution model Just et al. (1996) find I-K colors for the thin disks of edge-on galaxies to be ~ 1.2 mag, similar to the colors of a K3III star. While these models were not designed specifically for NGC 891, they are another indication that the NIR luminosity in Popescu et al. (2011) needs to be redistributed between the young and old stars.

5.2. Impact of the vertical fitting function

5.2.1. The luminosity profile and total light

As mentioned in Section 4.2.1, the functional form of the vertical light distribution has been much debated, with different authors favoring different indices of n in Equation 4. Due to dust obscuration near the midplane, shallow image depth, or both, most of the prior studies have only been able to accurately constrain fits with one (or at most two, when the data are deep enough to probe the thick disk) disk component(s). However, our data provides constraints for three disks, and while our 1- and 2-component exponential models produce smaller reduced χ^2 than the equivalent sech^2 model, our 3-component model results in sech^2 and exponential fits that are nearly indistinguishable from each other. This similarity is also seen in the inferred total luminosity ($L_{TOT} = L_{ST} + L_T + L_{Th}$) of the exponential model and the sech^2 model, where L_{ST} , L_T , and L_{Th} are the super-thin, thin and thick components respectively. Despite differences in individual component parameters $\frac{L_{TOT,exp}}{L_{TOT,sech^2}} = 1.00$. The same ratio for the 1- and 2-component models is ~ 1.15 and ~ 1.06 , respectively.

These result indicates (i) that the presence of multiple disk components must be considered when fitting the vertical light distribution; and (ii) a distinction between sech^2 and exponential fitting functions cannot be made in this context because when adequate components are introduced to fit the observed light distribution, the different functions are indistinguishable.

Due to the difficulty of statistically distinguishing between different empirical forms of the vertical surface brightness distribution, it could be argued that physically motivating a vertical profile from equations of dynamical equilibrium would lead to more accurate results. Comerón et al. (2011b) take this approach in their ver-

tical surface brightness profile fitting, and find theoretical values that seem to more closely resemble sech function, intermediate in concentration at small z between exponential or sech^2 functions. To test the sech distribution we performed a 2D partially fixed 3-component disk parameter fit to our K_s -band data (corrected with RT Model B) using this distribution. We find that all fitted free parameter values for the sech distribution fall between the fitted values from the equivalent model using the exponential and sech^2 distributions (see the 12th and 14th columns of Table 3), with a reduced χ^2 only 0.01 better than the corresponding sech^2 fit.

This result indicates that it is not necessary to compute dynamically consistent profiles in order to parameterize the light distribution of galaxy disks: empirical functions can be used with the same accuracy provided there are adequate components.

5.2.2. Component scales and scale ratios

It still might be argued, however, that dynamically self-consistent vertical profile functions would enable a more physical interpretation of the derived parameters characterizing the light profile. On the other hand, in light of Bovy et al. (2012)’s argument that disk components are likely continuous, extant dynamical analysis assuming discrete components may be misleading. Nonetheless, the observed vertical light profiles do appear to have clear breaks at 0.2 and 1.1 kpc, and this makes it reasonable to consider discrete components. As such, it is important to understand the systematics attributable to different choices for the vertical fitting function.

We find that for all of our models (1, 2, and 3-component) the cuspiest exponential vertical profiles yield larger scale-heights relative to sech^2 vertical profiles. Although both models adopt a radially exponential light distribution, models with exponential *vertical* profiles yield smaller *radial* scale-lengths. Combined, the disk oblateness changes by roughly a factor of 1.5 between models with vertical light profiles that are exponential or sech^2 , with disk models becoming apparently thinner for sech^2 vertical profiles. Again, this holds for all components in 1, 2, and 3-component models.

In the 3-component model the disk oblateness also changes more rapidly between thin and thick components (a factor of ~ 5) compared to the oblateness change between super-thin and thin components (a factor of ~ 2). These different oblateness changes are driven mostly by changes in the radial scale-length, which increases by almost a factor of 2 between super-thin and thin components, but only by $\sim 20\%$ between thin and thick components. In contrast the scale-height ratio for thin to super-thin components is $\frac{h_{z,T}}{h_{z,ST}} \sim 3.6(4.2)$ for the exponential (sech^2) fits while for thick to thin components the ratio is $\frac{h_{z,Th}}{h_{z,T}} \sim 5.0(5.8)$ for the exponential (sech^2) fits. Not surprisingly for our 2-component models the scale-height ratio for the two components is intermediate between the results for thin-to-superthin and thick-to-thin ratios.

The scale-height ratios for NGC 891 think-to-thin components are comparable to those found by Comerón et al. (2011b), based on thin-thick disk decompositions of edge-on spirals in the S⁴G survey, for morphological type T = 3 (Hyperleda indicates NGC 891 has T = 3.1 ± 0.4). The

good agreement of our results for thin and thick disk thickness ratios to those of Comerón et al. (2011b), who only fit two disks to their data, indicates either that the presence of unaccounted-for flux from super-thin disks does not significantly bias their results for the ratios of scale-heights of thin and thick components or that most of their sample is without super-thin disk components.

Changes in relative component luminosities are more subtle. For the ease of the following discussion we tabulate the component luminosities of the exponential and sech^2 fits with three disk components in Table 5. For 3-component models, regardless of the functional forms of the vertical light profile and whether there is a truncation, the thin component contributes the most to the total disk luminosity, followed by the super-thin component, and last the thick component. (In the 2-component model it is also the case that the second component, most closely identified with the thin disk, also contributes the most light.) If we take the difference between the exponential and sech^2 values as characteristic of the systematic errors then we find the three disk components, thin, super-thin and thick, contribute $51\pm 4\%$, $34\pm 4\%$, $15\pm 1\%$, respectively. The systematic error in the thick-disk component luminosity is likely underestimated because this component was fixed in scale-height and scale-length.

The most striking change in relative luminosities occurs between superthin and thin disks in our three-component fits to NGC 891, with the exponential model having $\frac{L_{ST}}{L_T} \sim 0.5$ compared to $\frac{L_{ST}}{L_T} \sim 0.8$ for the sech^2 model. This comes about despite the scale-height and scale-length ratios between superthin and thin components being the same for both exponential and sech^2 models. What drives the difference in component luminosity is a change in relative surface-brightness. In contrast to the superthin-to-thin luminosity ratio, the luminosity ratios of thick-to-thin components is $\frac{L_{Th}}{L_T} \sim 0.3$, i.e., essentially unchanged for exponential, sech^2 or the truncated sech^2 models.

The relatively constancy of thick-to-thin luminosities is interesting given that Comerón et al. (2011b) report a systematic variation in $\frac{L_{Th}}{L_T}$ when using different functional forms of the vertical surface brightness profile, which they argue arises as a result of how rounded (or concentrated) the model light profiles are near the mid-plane. Specifically, they find thick-to-thin component luminosity ratios 60% larger than Yoachim & Dalcanton (2006). The latter adopt a sech^2 vertical profile, less concentrated than that adopted by Comerón et al. (2011b), which is closer to a sech function. The fact that we obtain similar $\frac{L_{Th}}{L_T}$ ratios for both our fitting functions might indicate that the addition of a super-thin disk component removes this discrepancy. However, even for our 2-component disk fits, the luminosity ratios only vary by 4%, so something else must be going on.

As an exercise, we took the sech^2 vertical profiles fit for Yoachim & Dalcanton (2006)'s sample, and fit to the sum of these components two new 2-component models, one where both components have sech vertical light profiles, and the other where both components have exponential vertical light profiles. We found that the luminosity ratios for the sech vertical profiles were roughly

60% larger than those for the input model sech^2 vertical profiles (the exponential vertical profiles were 60% larger again relative to the ratios for the sech vertical profiles). This is the same factor found by Comerón et al. (2011b). Both our exercise here and Comerón et al. (2011b)'s are one-dimensional fits (in z only). Our conclusion is that the difference in thick-to-thin luminosity ratios is an artifact of one-dimensional fitting which is largely eliminated when two-dimensional light-profiles fits are performed.

5.3. MIR Vertical Profiles

Of value to our investigation would be corroborating evidence of a super-thin disk in NGC 891 in another dataset, ideally in the MIR which has been claimed to be ideal for studies of starlight with minimal attenuation (Sheth et al. 2010). Towards that end we analyzed the archival IRAC $4.5\mu\text{m}$ data looking for a super-thin component consistent with our NIR fits. While the IRAC data has resolution only half that of the lowest resolution of our WHIRC data, we note that our K_s -band fits indicate that NGC 891's super-thin disk has a central surface brightness $\sim 1.5\text{-}2$ mag arcsec $^{-2}$ brighter than its thin disk, and ~ 4 mag arcsec $^{-2}$ brighter than its thick disk. At 4 kpc in radius and at the approximate resolution of the IRAC data in height ($1.8'' \sim 80$ pc), the super-thin disk surface brightness should be comparable to the fitted thin disk surface brightness (~ 0.2 mag fainter for the exponential fit, and ~ 0.9 mag brighter for the sech^2 fit, assuming no color gradients between K_s and $4.5\mu\text{m}$). Therefore it is not unreasonable to expect to see at least some evidence of the super-thin disk in the IRAC data, even though it may never be the dominant component in the ranges we can probe.

We computed 2D fits to the IRAC $4.5\mu\text{m}$ data, using the same methodology as our fits of the K_s -band WHIRC data, with a 3-component disk model. The exponential disk model had difficulty converging on a physically plausible fit, due to degeneracies introduced by the lowered resolution. The sech^2 model, however, produced a good fit (Table 6 and Figure 22) with parameters very similar to that for the K_s -band data. The scale-heights of the super-thin and thin disk in the fits to the $4.5\mu\text{m}$ data are identical to the K_s -band values.

In hindsight it is perhaps unsurprising that we were able to identify NGC 891's super-thin disk at $4.5\mu\text{m}$: Comerón et al. (2011b) set out to decompose the galaxies in the S⁴G sample into thin and thick disk components, but several (e.g. IC 2058, NGC 1495, and NGC 5470) have fits that are closer to what would be expected for a super-thin+thin disk. This suggests not only that the IRAC bands are capable of identifying super-thin disks in (very) nearby galaxies, but that such disks may be common in the local universe. Attempting a 3-component decomposition of these S⁴G galaxies would be a logical next step in determining if they are truly super-thin+thin+thick disk systems. Indeed, Comerón et al. (2011a) perform a 3-component (1D) analysis on S⁴G data of NGC 4013, and find a system that appears to have a MW-like super-thin disk but extended (in height) thin and thick disks. Comerón et al. (2011a) do not identify the narrowest disk as a super-thin disk but rather term the components thin, thick, and 'extended'; this difference is semantic until there is a clear astrophysical

TABLE 5
MODEL B THREE DISK MODEL TOTAL LUMINOSITIES ($L/L_{\odot,K}$)^a

	exp	No Truncation		Truncated, with Bar + Nuclear Disk	
		% ^b	sech ²	% ^b	sech ²
L_{ST}^c	5.05×10^{10}	29	6.62×10^{10}	38	4.04×10^{10}
L_T^c	9.60×10^{10}	55	8.41×10^{10}	48	6.86×10^{10}
L_{Th}^c	2.85×10^{10}	16	2.52×10^{10}	14	2.13×10^{10}
L_{bar}	2.49×10^{10}
L_{nuc}	8.32×10^9
L_{tot}	1.75×10^{11}	100	1.76×10^{11}	100	1.64×10^{11}

^a $L_{\odot,K} = 3.909 \times 10^{11} WHz^{-1}$ from Binney & Merrifield (1998).

^b Percentage of total luminosity for each component.

^c ST, T, and Th are equivalent to disk components 1,2, and 3 in Table 3.

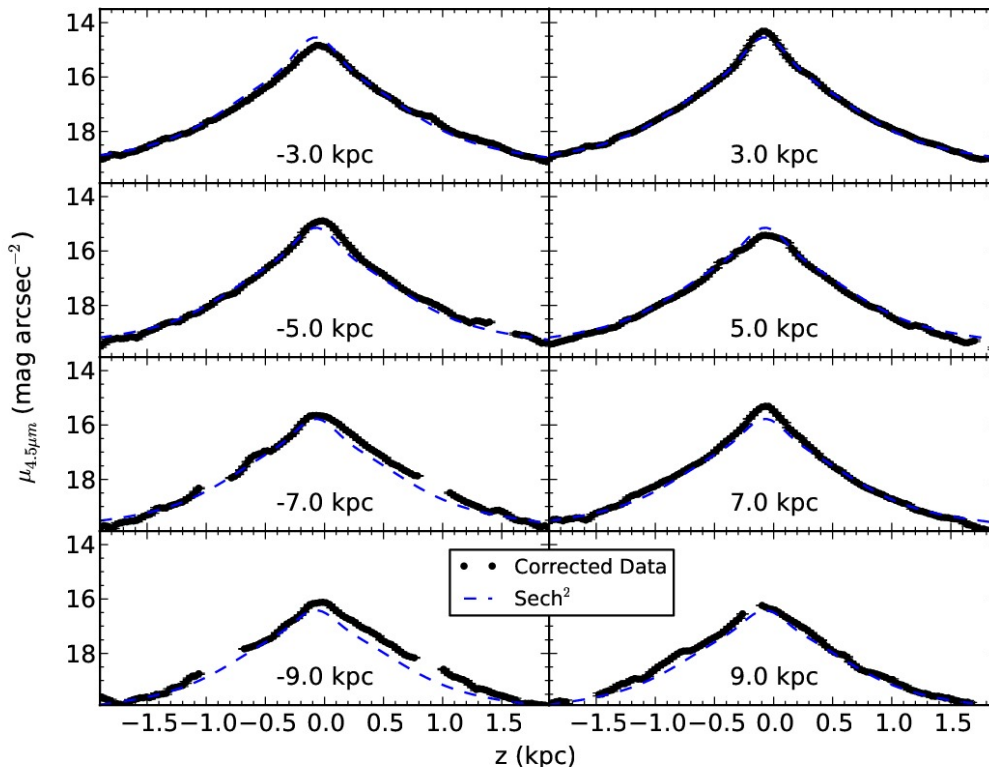


FIG. 22.— Three-component sech² model vertical profiles (blue lines), overlaid on the IRAC 4.5 μ m data (black points), at several radii. Gaps in the data are due to foreground stars which were removed before plotting. There are more gaps than for the WHIRC data (Figures 16-18) due to a combination of very red stars and the increased size of the IRAC point-source function, which spreads more light from nearby stars near (but not in) our apertures into the profiles. Positive radii are on the SW side of the galaxy.

distinction between the components (e.g. age).

Although the lower-resolution IRAC data appears good enough to identify super-thin disks in at least some nearby edge-on galaxies there are still several advantages to our methodology. First and foremost is the increased resolution in the NIR, which allows super-thin disks to be constrained at much larger distances. This is especially important for the study of MW-sized galaxies, which are relatively rare in the local universe. The increased resolution is helpful even in nearby galaxies: lower spatial resolution increases the likelihood of degeneracies in the

fits, which is already known to be an important issue in performing edge-on disk decompositions (Morrison et al. 1997). The primary motivation for undertaking vertical disk decompositions in the MIR is the limited dust attenuation at those wavelengths and the availability of deep imaging data from *Spitzer*. However, our radiative transfer models indicate there is as much as 0.5 mag of attenuation at 4.5 μ m (Figures 12 and 14). While most of the 4.5 μ m light experiences very little attenuation given the concentration of dust near the midplane, a full, accurate accounting of the MIR light will **still** require an

TABLE 6
IRAC 4.5 μ m MODEL
PARAMETERS

Parameter ^a	sech ²
$\mu_{0,1}$	13.97 \pm 0.032
$h_{R,1}$	2.39 \pm 0.016
$h_{z,1}$	0.06 \pm 0.002
$\mu_{0,2}$	15.21 \pm 0.012
$h_{R,2}$	3.50 \pm 0.007
$h_{z,2}$	0.25 \pm 0.001
$\mu_{0,3}$	18.26 \pm 0.003
$h_{R,3}$	4.80 ^b
$h_{z,3}$	1.44 ^b

^a μ values in mag arcsec⁻¹,
 h_R , h_z values in kpc.

^b Fixed values from
Ibata et al. (2009).

attenuation correction.

Further, by using K_s-band data we ensure that we exclusively fit the light from the stellar disk(s) and avoid contamination from dust, which Meidt et al. (2012) find to be $\geq 5\%$ of total integrated light and up to 20% of the light locally from star-forming regions in spiral galaxies. While MIR dust emission does affect our attenuation correction in the K_s-band by skewing the K_s-4.5 μ m color, this is a second-order effect — a correction to a correction in the K_s-band itself. The ability of our model to reproduce the data at a variety of radii and heights (Figure 5) indicates that it has been properly accounted for in our modeling. In contrast, dust emission is both a first and second order correction at 3.6 and 4.5 μ m.

Finally, there is additional value in making the attenuation correction in the NIR as it opens up this important spectral region for future imaging and spectroscopic efforts. For instance, there are several molecular bandheads between 1 and 2.3 μ m which may be able to separate different types of cold giant stars (Lançon et al. 2007), allowing for age and composition gradients to be determined in the stellar disks.

6. CONCLUSION

We have obtained sub-arcsecond resolution NIR imaging of NGC 891, a nearby massive spiral galaxy frequently compared to the Milky Way, using the WHIRC instrument on the WIYN telescope. These images cover roughly ± 10.5 kpc in radius and all relevant regions for vertical disk decompositions. We reduced the data using our own pipeline, specifically designed for the reduction of images with very extended sources. We supplemented this data with archival *Spitzer* IRAC 3.6 and 4.5 μ m data, primarily to assist in computing an attenuation correction.

Concurrently, we produced a 3D Monte Carlo RT SED model of NGC 891 using parameters known to fit the UV-FIR SED of the galaxy. A comparison of the IR colors predicted by the model with our WHIRC and IRAC data indicated that the balance of dust grain sizes was different near the midplane compared to at large heights. We therefore constructed a second model with a lowered PAH fraction near the midplane, which provided better fits to the data at small heights while leaving the color distribution at large heights unchanged. Both of these

models were used to construct an attenuation correction based on the K_s-4.5 μ m color. The difference in the attenuation correction between the two models is small (to first order the difference starts at 0 mag, increases at a rate of ~ 0.4 mag per mag of K_s-band attenuation up to $A_{K_s}^e = 1.5$ mag, then increases at a much smaller rate of ~ 0.07 mag per magnitude of attenuation) and does not significantly affect the following results.

Using a Levenberg-Marquardt nonlinear curve fitting routine, we fit 2D seeing-convolved surface-brightness profiles to the K_s-band data, using models with up to three disk components. The vertical light distributions of the disks were parameterized by either exponential or sech² functions, while the radial distributions were assumed to be exponential. It is immediately clear that single disk component models provide poor fits to the data. Two- and 3-component models do much better, and a close inspection of the vertical profiles shows that three components are necessary to fully model the light distribution. The 3-component model produces a *thin* disk with scale-length (h_R) ~ 4 kpc and scale-height (h_z) ~ 0.27 kpc, and a *super-thin* disk with h_R and h_z of ~ 2.1 kpc and ~ 0.07 kpc respectively. The thin and super-thin disks are consistent with prior work on NGC 891 and the MW's young, star-forming disk (albeit with a smaller scale-length). We find that as h_z decreases from the thick to the super-thin disk the oblateness ($\frac{h_R}{h_z}$) increases from ~ 3 to ~ 30 , even though h_R is also decreasing. Without data sensitive to star-formation rate we cannot definitively state that NGC 891's super-thin disk is star-forming like its putative Milky Way counterpart, but this does seem to be the most likely possibility, particularly given the evidence for embedded star-formation from the observed FIR excess in this galaxy.

While our 3-component models fit the data well outside of the central bulge region, near the center of NGC 891 this model produces significant residuals with respect to the data, overestimating the light near the midplane while underestimating light away from the midplane. These residuals are consistent with what would be expected from a bar. CO observations have indicated that NGC 891 has a bar, and the presence of such a structure is clear from X-shaped isophotes visible in our data, which are characteristic of bar orbits. The simplest explanation consistent with the data is that NGC 891's bar truncates the galaxy's main disk components and redistributes the stars into the bar structure. Other than the relatively low surface-brightness X-shaped isophotes the bar appears to be well fit by a disk with a scale-length of ~ 1.3 kpc and a scale-height of ~ 0.4 kpc.

We also find excess light at the very center of NGC 891. This excess is well fit by a nuclear disk with the same scale-height as the super-thin disk, a scale-length of 0.25 kpc ($\sim 10\%$ of the super-thin disk), and 20% of the super-thin disk's luminosity; a classical $R^{1/4}$ -law bulge cannot adequately fit this feature and in fact this type of spheroid does not appear to be present at all in NGC 891.

A truncation between the central components (the nuclear disk and bar) and the three main disks is also necessary to accurately model the entire K_s-band light distribution of NGC 891. This truncation happens at roughly

3.1 kpc. New models with this nuclear disk, a rough approximation to the bar, and a disk/bar truncation are able to produce good fits to our data all the way down to the center of NGC 891.

We find that when three disk components are modeled, both exponential and sech^2 vertical distribution functions fit the data equally well, even at our sub-arcsecond resolution. Despite the apparent difference in individual fitted parameters between the sech^2 and exponential 3-component disk model (e.g. sech^2 disks tend to have smaller scale-heights than exponential disks), we find that they predict nearly identical *total* K_s -band luminosities for NGC 891 (models with fewer components predict slightly larger total luminosities for the exponential disks, on the order of $\sim 10\%$). The sech^2 disk model including the bar, nuclear disk, and disk/bar truncation has comparable total luminosity, $\sim 95\%$ as bright as the simpler 3-component disk model with no truncation. Based on the truncated model we find that the super-thin component (including the nuclear disk) contributes roughly 30% of the total K_s -band luminosity in NGC 891, while the thin disk, thick disk, and bar respectively contain $\sim 42\%$, 13%, and 15% of the total. The luminosity and scale height ratios of NGC 891's thin and thick disk agree with those found for other edge-on spirals in the S⁴G study of comparable type and rotation speed, even though the S⁴G analysis only fits two disks to their data.

The K_s -band luminosity of NGC 891's super-thin disk is a factor of 4-10 larger than what has been adopted in radiative transfer models capable of reproducing the UV-FIR integrated SED of the galaxy (Bianchi 2008; Popescu et al. 2011). The *total* disk luminosity is, however, very similar between these models and our results. The most likely explanation for this discrepancy is that some of the NIR light that had been attributed to the thin+thick disks in these earlier models actually belongs to the super-thin component. Prior to the present work NGC 891's super-thin disk had never been directly detected, and although its UV luminosity could be inferred by using energy-balance arguments, there were no direct constraints on its luminosity in the NIR or its spatial location. Because the UV luminosity of the super-thin disk *is* fairly well constrained, the additional NIR light seen in our data cannot be accounted for by uniformly increasing the intrinsic super-thin disk luminosity at all wavelengths. Rather, the NIR luminosity must be boosted without affecting the intrinsic super-thin disk SED in the UV, likely through an increased amount of cool evolved stars, such as RSGs and AGBs. Confirmation of this conjecture will be the topic of a future paper.

Finally, we determine that there is also an excess of

light near NGC 891's midplane in IRAC 4.5 μm data, with scale height comparable to what we find for the super-thin disk in the NIR. However, while useful for verifying the validity of our methodology, there are several reasons why IRAC data are non-ideal for identifying super-thin stellar disks. First, contemporary NIR instruments yield much higher angular resolution than their MIR counterparts; NIR detectors will be able to probe super-thin disks at larger distances from the MW. Secondly, we have shown that the IRAC bands have up to ~ 0.5 mag of dust attenuation near the midplane on NGC 891. Therefore, any attempt to determine the intrinsic light profile from a spiral galaxy's disk at low heights will need to employ an attenuation correction like the one derived in this work, even in the MIR. Finally, both the IRAC 3.6 and 4.5 μm filters (the ones most commonly used to measure stellar flux) have non-negligible amounts of non-stellar emission from PAH and hot dust particles. Any attempt to compute the stellar flux at these wavelengths must therefore correct for this emission, which is known to be highly variable across individual galaxies. By combining our NIR observations with existing MIR data, we are able to probe deeper than if we used each wavelength regime independently: We retain the spatial resolution and minimal susceptibility to contamination from dust emission of the NIR, while producing excellent attenuation corrections using the combination of the NIR and the MIR colors.

This research was supported by NSF AST-1009471. We thank Arthur Eigenbrot for assistance with the observations, Dick Joyce for useful conversations about optimizing WHIRC efficiency, and Jeff Percival for help with creating the dither scripts used for the observations. We also acknowledge Tom Robitaille, Barb Whitney, and Kenny Wood for assistance with the radiative transfer modeling and the dust physics. Discussions with Bob Benjamin were very useful in comparing the disk components to those in the MW. We also thank Blakesley Burkhardt and Corey Wood for helpful edits and revisions. Comments from an anonymous referee were also very useful in improving this work. We acknowledge the usage of the HyperLeda database (<http://leda.univ-lyon1.fr>). This work is based in part on observations made with the Spitzer Space Telescope, obtained from the NASA/IPAC Infrared Science Archive, both of which are operated by the Jet Propulsion Laboratory, California Institute of Technology under a contract with the National Aeronautics and Space Administration.

REFERENCES

- Anderson, K. S. J., Baggett, S. M., & Baggett, W. E. 2004, *AJ*, 127, 2085
- Aoki, T. E., Hiromoto, N., Takami, H., & Okamura, S. 1991, *PASJ*, 43, 755
- Bahcall, J. N., & Soneira, R. M. 1980, *ApJS*, 44, 73
- Banerjee, A., & Jog, C. J. 2007, *ApJ*, 662, 335
- Barnaby, D., & Thronson, H. A., Jr. 1992, *AJ*, 103, 41
- Barteldrees, A., & Dettmar, R.-J. 1994, *A&AS*, 103, 475
- Bershady, M. A., Verheijen, M. A. W., Swaters, R. A., et al. 2010, *ApJ*, 716, 198
- Bershady, M. A., Verheijen, M. A. W., Westfall, K. B., et al. 2010, *ApJ*, 716, 234
- Bershady, M. A., Martinsson, T. P. K., Verheijen, M. A. W., et al. 2011, *ApJ*, 739, L47
- Bertin, E., & Arnouts, S. 1996, *A&AS*, 117, 393
- Bertin, E., Mellier, Y., Radovich, M., et al. 2002, *Astronomical Data Analysis Software and Systems XI*, 281, 228
- Bertin, E. 2006, *Astronomical Data Analysis Software and Systems XV*, 351, 112
- Bessell, M. S., & Brett, J. M. 1988, *PASP*, 100, 1134
- Bianchi, S. 2008, *A&A*, 490, 461
- Binney, J., & Merrifield, M. 1998, *Galactic astronomy / James Binney and Michael Merrifield*. Princeton, NJ : Princeton University Press, 1998.
- Bovy, J., Rix, H.-W., & Hogg, D. W. 2012, *ApJ*, 751, 131
- Bureau, M., & Freeman, K. C. 1999, *AJ*, 118, 126
- Bureau, M., Aronica, G., Athanassoula, E., et al. 2006, *MNRAS*, 370, 753

- Calzetti, D., Kinney, A. L., & Storchi-Bergmann, T. 1994, *ApJ*, 429, 582
- Cardelli, J. A., Clayton, G. C., & Mathis, J. S. 1989, *ApJ*, 345, 245
- Cohen, M., Wheaton, W. A., & Megeath, S. T. 2003, *AJ*, 126, 1090
- Combes, F., & Sanders, R. H. 1981, *A&A*, 96, 164
- Combes, F., Debbasch, F., Friedli, D., & Pfenniger, D. 1990, *A&A*, 233, 82
- Comerón, S., Elmegreen, B. G., Knapen, J. H., et al. 2011, *ApJ*, 738, L17
- Comerón, S., Elmegreen, B. G., Knapen, J. H., et al. 2011, *ApJ*, 741, 28
- Dalcanton, J. J., & Bernstein, R. A. 2000, *AJ*, 120, 203
- Dalcanton, J. J., Yoachim, P., & Bernstein, R. A. 2004, *ApJ*, 608, 189
- de Grijs, R., & van der Kruit, P. C. 1996, *A&AS*, 117, 19
- de Grijs, R., Peletier, R. F., & van der Kruit, P. C. 1997, *A&A*, 327, 966
- Draine, B. T., & Li, A. 2007, *ApJ*, 657, 810
- Fazio, G. G., Hora, J. L., Allen, L. E., et al. 2004, *ApJS*, 154, 10
- Floc, M., & Rocca-Volmerange, B. 1997, *A&A*, 326, 950
- García-Burillo, S., & Guélin, M. 1995, *A&A*, 299, 657
- Holwerda, B. W., Bianchi, S., Böker, T., et al. 2012, *arXiv:1204.2936*
- Ibata, R., Mouhcine, M., & Rejkuba, M. 2009, *MNRAS*, 395, 126
- Indebetouw, R., Mathis, J. S., Babler, B. L., et al. 2005, *ApJ*, 619, 931
- Johnson, H. L. 1966, *ARA&A*, 4, 193
- Joye, W. A., & Mandel, E. 2003, *Astronomical Data Analysis Software and Systems XII*, 295, 489
- Just, A., Fuchs, B., & Wielen, R. 1996, *A&A*, 309, 715
- Kamphuis, P., Holwerda, B. W., Allen, R. J., Peletier, R. F., & van der Kruit, P. C. 2007, *A&A*, 471, L1
- King, I., Gilmore, G., & van der Kruit, P. C. 1990, *The Milky Way as a Galaxy*
- Kissler-Patig, M., Pirard, J.-F., Casali, M., et al. 2008, *A&A*, 491, 941
- Lançon, A., & Mouhcine, M. 2002, *A&A*, 393, 167
- Lançon, A., Hauschildt, P. H., Ladjal, D., & Mouhcine, M. 2007, *A&A*, 468, 205
- MacLachlan, J. M., Matthews, L. D., Wood, K., & Gallagher, J. S. 2011, *ApJ*, 741, 6
- Maraston, C. 2005, *MNRAS*, 362, 799
- Martin, C. L., & Kennicutt, R. C., Jr. 2001, *ApJ*, 555, 301
- Martinsson, T. P. K., Verheijen, M. A. W., Westfall, K. B. W. et al. 2013, *A&A*, submitted
- Matthews, L. D., & Wood, K. 2001, *ApJ*, 548, 150
- Meidt, S. E., Schinnerer, E., Knapen, J. H., et al. 2012, *ApJ*, 744, 17
- Meixner, M., Smee, S., Doering, R. L., et al. 2010, *PASP*, 122, 451
- Mihos, J. C., Walker, I. R., Hernquist, L., Mendes de Oliveira, C., & Bolte, M. 1995, *ApJ*, 447, L87
- Morrison, H. L., Boroson, T. A., & Harding, P. 1994, *AJ*, 108, 1191
- Morrison, H. L., Miller, E. D., Harding, P., Stinebring, D. R., & Boroson, T. A. 1997, *AJ*, 113, 2061
- Oosterloo, T., Fraternali, F., & Sancisi, R. 2007, *AJ*, 134, 1019
- Pierini, D., Gordon, K. D., Witt, A. N., & Madsen, G. J. 2004, *ApJ*, 617, 1022
- Popescu, C. C., Misiriotis, A., Kylafis, N. D., Tuffs, R. J., & Fischera, J. 2000, *A&A*, 362, 138
- Popescu, C. C., Tuffs, R. J., Dopita, M. A., et al. 2011, *A&A*, 527, A109
- Povich, M. S., Stone, J. M., Churchwell, E., et al. 2007, *ApJ*, 660, 346
- Pritchett, C., & Kline, M. I. 1981, *AJ*, 86, 1859
- Raha, N., Sellwood, J. A., James, R. A., & Kahn, F. D. 1991, *Nature*, 352, 411
- Rice, W., Merrill, K. M., Gatley, I., & Gillett, F. C. 1996, *AJ*, 112, 114
- Robitaille, T. P. 2011, *A&A*, 536, A79
- Schechtman-Rook, A., Bershady, M. A., & Wood, K. 2012, *ApJ*, 746, 70
- Schechtman-Rook, A., Bershady, M. A., Wood, K., & Robitaille, T. P. 2012, *IAU Symposium*, 284, 104
- Schechtman-Rook, A., & Hess, K. M. 2012, *arXiv:1203.1319*
- Seth, A. C., Dalcanton, J. J., & de Jong, R. S. 2005, *AJ*, 130, 1574
- Sheth, K., Regan, M., Hinz, J. L., et al. 2010, *PASP*, 122, 1397
- Spitzer, L., Jr. 1942, *ApJ*, 95, 329
- Tokunaga, A. T. 2000, *Allen's Astrophysical Quantities*, 143
- van Albada, T. S., Bahcall, J. N., Begeman, K., & Sancisi, R. 1985, *ApJ*, 295, 305
- van der Kruit, P. C. 1988, *A&A*, 192, 117
- van der Kruit, P. C., & Searle, L. 1981, *A&A*, 95, 105
- van der Kruit, P. C., & Searle, L. 1981, *A&A*, 95, 116
- van Dokkum, P. G., Peletier, R. F., de Grijs, R., & Balcells, M. 1994, *A&A*, 286, 415
- Wainscoat, R. J., Freeman, K. C., & Hyland, A. R. 1989, *ApJ*, 337, 163
- Walcher, J., Groves, B., Budavári, T., & Dale, D. 2011, *Ap&SS*, 331, 1
- Weingartner, J. C., & Draine, B. T. 2001, *ApJ*, 548, 296
- Werner, M. W., Roellig, T. L., Low, F. J., et al. 2004, *ApJS*, 154, 1
- Westfall, K. B., Bershady, M. A., Verheijen, M. A. W., et al. 2011, *ApJ*, 742, 18
- Wright, E. L., Eisenhardt, P. R. M., Mainzer, A. K., et al. 2010, *AJ*, 140, 1868
- Xilouris, E. M., Alton, P. B., Davies, J. I., et al. 1998, *A&A*, 331, 894
- Xilouris, E. M., Byun, Y. I., Kylafis, N. D., Paleologou, E. V., & Papamastorakis, J. 1999, *A&A*, 344, 868
- Yoachim, P., & Dalcanton, J. J. 2006, *AJ*, 131, 226
- Zasowski, G., Majewski, S. R., Indebetouw, R., et al. 2009, *ApJ*, 707, 510

APPENDIX

WHIRC DATA REDUCTION PROCEDURE

Initial Data Inspection

Before (and during) the data reduction process we inspected the individual images for artifacts and defects. Three images from both the SW and NE K_s -band pointings contained elevated signal levels over a large region near the left-middle of the detector and were removed from the reduction. Additionally, during a few exposures of the central K_s -band and SW H-band the sky background appears to undergo a rapid change, faster than our sky-source duty cycle. We therefore also removed four SW H-band exposures and five central K_s -band exposures from the reduction pipeline.

Individual Image Reduction

Data reduction generally followed the procedures described in the WHIRC Quick Guide to Data Reduction manual⁹, although we modified several steps to optimize the reduction for very extended targets like NGC 891. We detail all reduction steps here for clarity, going into depth for the non-standard portions of our reduction.

First, excess data on the images were trimmed off. Then, images taken with Fowler-4 sampling (J-band) were divided by four to remove the additive nature of the sampling. We then applied a linearity correction to all images with the IRAF task IRLINCOR using coefficients provided in the data reduction manual. The coordinate matrix of the image headers was then adjusted to take into account the rotation of the telescope during the observations.

We took 20 dome flat exposures for each filter: 10 with the dome lamps on and 10 with the lamps off. The 10 lamp-on flat images were scaled to have the same mean flux in the central quarter of the images and then averaged

⁹ http://www.noao.edu/kpno/manuals/whirc/WHIRC_Datared_090824.pdf

together to produce a combined lamp-on flat; this process was then repeated with the lamp-off flats. The combined lamp-off flat was then subtracted from the combined lamp-on flat to remove any signal not coming from the flat lamps (e.g. dark current, scattered light, or thermal emission in the dome).

Before reducing the flat-fields any further, a first-order correction must be applied because WHIRC has a ‘pupil ghost’, likely due to internal reflections in the imager’s optics. It appears in the central 80'' of the detector. This feature is most prominent in the K_s -band, with an amplitude about 15% of the background, but it is also present (albeit at much lower levels) in J and H as well. The ghost was modeled and removed from the flat-fields (it is removed from the object frames naturally during the sky-subtraction process) using the representative pupil template provided on the WHIRC web page¹⁰ and the IRAF MSCRED.RMPUPIL task. While pupil templates can be constructed from J and K_s flats, for our purposes the provided template was more than adequate, with errors <0.3% on the corrected images. We note that the flats we used are from an earlier night in our run (UT date 2011 Oct 16); we found night-to-night deviations in the flat-fields of <1% over the entire image area. All object and sky images were flattened before proceeding with further data processing.

Finally, the central quarter of the pupil-ghost-removed flat was normalized to an average value of 1. Small and negative pixel values (caused by bad pixels and later masked out) were replaced by unity, to prevent erroneously large and/or negative flux values from appearing in the flat-fielded science images.

Sky Subtraction

With extended sources like NGC 891, sky subtraction can be very difficult. To combat this problem, we interleaved observations of a relatively empty sky field $\sim 10'$ away (with similar dither amplitudes between sky images as for the data) with our observations of NGC 891. For each set of on-source dithers (4 for J and H, 9 for K_s) we combine sky images taken before (2 for J and H, 5 for K_s) and after (again, 2 for J and H and 5 for K_s) to produce a sky frame suitable for use on the data images. Each sky frame was scaled to have the same median value to avoid biasing the statistics. The sky frames were then median combined iteratively pixel-by-pixel with 2σ clipping until the median converged or all the pixels in the individual sky frames had been clipped out.

After all pixels have been median combined, we used an iterative relaxation algorithm (described in Appendix B) to interpolate sky values for sky image pixels where all the constituent pixels were clipped out. The relaxation procedure provides accurate interpolation and converges very quickly when the pixels needing interpolation are relatively few and widely spaced; we deliberately chose to obtain dedicated sky images and ensured that dither amplitudes were larger than the stellar point-source-functions (PSFs) in order to make this process as efficient and accurate as possible. For a given set of on-source images the appropriate combined sky frame was scaled to have the same median value as the data frame and then subtracted. The resulting sky-subtracted image was then field flattened by the normalized flat-field image.

Prior to registration, the sky-subtracted data images were cleaned of (most) chip defects using the IRAF task FIXPIX (a linear interpolator) and a pixel mask created from the ratio of two lamp-on flats with different exposure times. The data images were then distortion corrected using the IRAF task GEOTRAN and distortion files downloaded from the WHIRC web page.

WHIRC has a very small dark current (~ 0.2 DN sec^{-1} pix^{-1}) compared to the sky background in most filters. For comparison, WHIRC J-band has an average sky brightness of ~ 6 DN sec^{-1} pix^{-1} . (Dark current is not an issue even in principle for dome flats since we utilize ‘on-off’ differences.) Additionally, the sky subtraction procedure functions to remove most of the (already small) contribution to the image flux from the dark current. However, the dark current exhibits a fixed pattern structure. Further, the correct procedure for dark current removal is subtraction *before* field-flattening. Nonetheless, due to our limited set of dark frames, we were unable to demonstrate an improvement in image flatness with dark subtraction. Therefore a separate dark subtraction has minimal impact on the reduced images. For future studies focusing on low surface-brightness extended structure we do recommend a more thorough investigation of dark-current subtraction.

When compared to a super-sky frame made up of an average of a given night’s sky images, the dome flats appear to have small (on the order of 1%) illumination errors. However, the illumination appears to vary between nights and potentially even during nights, making correction difficult. We tested an illumination correction on a small subset of our data and found it made very little difference in the reduced images. Due to the limited improvement and variability of the illumination we do not employ an illumination correction, but again we recommend a more careful exploration of this issue for detailed low surface-brightness studies.

Relative Image Registration and Mosaics

Because of WHIRC’s relatively small field of view and the extremely extended nature of NGC 891 on the chip, fully automatic registration procedures (e.g. SCAMP; Bertin 2006) were found to be unreliable. Therefore we performed relative image registration between individual exposures by hand, first computing source catalogs for each image using Source Extractor (Bertin & Arnouts 1996), then hand-identifying individual sources that overlapped between images. Based on visual comparisons between individual registered images and the PSF of the final mosaics, our registration scheme is accurate to $\lesssim 1$ pixel.

With the images all registered in relation to each other, we created full J, H, and K_s mosaics using the Swarp software package (Bertin et al. 2002). Because of the extended nature of NGC 891 compared to the WHIRC field-of-view the

¹⁰ <http://www.noao.edu/kpno/manuals/whirc/dated.html>

estimate of the average flux in the individual data frames used to subtract the combined sky frame is biased, and therefore the background of the sky-subtracted images is over-subtracted. To combat this, we used the high S/N image mosaics to hand-produce very conservative masks of NGC 891 (and foreground stars), essentially masking out all pixels except those very close to the edge of the mosaic where galaxy contamination is minimized. This global mask was then converted into a pixel mask for each individual frame. We then re-ran the pipeline, starting from the sky-subtraction step, this time normalizing the sky images to the source images using only unmasked pixels. The relative WCS offsets were held constant from the first iteration of the pipeline. This two-step process effectively removes the over-subtraction bias from the extended nature of NGC 891 in our images.

Absolute WCS Registration and Flux Calibration

The next step was to register the image mosaics in an absolute astrometric system. First we hand-constructed catalogs of the centroids of stars visible on both the WHIRC K_s -band image and the IRAC $4.5 \mu\text{m}$ image (see Section 2.2 for details on the IRAC images) using Ds9 (Joye & Mandel 2003). Using the IRAC image as an astrometric reference is useful not only because we will be using K_s -IRAC colors in our analysis and therefore want good registration between these datasets but also because both the IRAC and WHIRC data go much deeper than standard NIR calibration catalogs. We then used the IRAF task CCMAP to perform the registration. To preserve the excellent relative agreement between bands the K_s -band absolute calibration was applied manually to the J and H bands.

To flux calibrate the images, stars from the 2MASS PSC with reliable photometry were matched to Source Extractor integrated fluxes on the mosaics. We then fit the relationship between $\log(\text{DN})$ and Vega magnitude, obtaining fits with standard errors of 0.02 (0.03, 0.02) mag in the J (H, K_s) bands.

ITERATIVE RELAXATION ALGORITHM

When stacking dithered images together to produce a sky frame, the ideal situation is to have enough exposures so that every pixel on the stacked frame has a large number of samples of the sky background with which to do statistics. In reality, however, even for relatively sparse fields it is not uncommon to find a few pixels on the stacked frame which were masked out on all of the input individual images, usually due to foreground or background contaminants appearing at multiple dither positions. For these pixels the sky background must be interpolated. As long as this happens only to a small fraction of the total field, we can still construct a very accurate sky background using our iterative relaxation method, described below.

For each ‘problematic’ pixel we first find the nearest pixel with a valid sky value, and use that value as an initial guess. Then, the average value of all adjacent pixels (including bad pixels) is computed, with pixels diagonally adjacent given weights of $1/\sqrt{2}$ the weights of horizontally and vertically adjacent pixels. The weighted average then becomes the next guess for the pixel value, and the difference between the initial guess and the weighted average is computed. This process iterates for all problematic pixels until the average change per pixel between iterations is below 1%. When the bad pixels are surrounded (or nearly surrounded) by good pixels, this process converges in just a few iterations. While our dither strategy minimizes source overlap on multiple dithers, it is not perfect and there are a few regions with multiple adjacent bad pixels. Generally, however, convergence occurs in under 100 iterations.

ATTENUATION FITTING SCHEME AND FORMULAE

To construct an attenuation correction we fit a curve to the projected image pixels of the RT model. Because the attenuation curve is relatively complex, we employ a piecewise approach to accurately fit the attenuation without relying on very high-order functions, which can have undesirable edge behavior.

For $K_s\text{-}4.5\mu\text{m} \lesssim 1.5$ mag we find that a fourth order polynomial fits the model trends of A_λ^e versus color quite well. For larger values of the attenuation we approximate the relationship as a line. To avoid any bias near the endpoints of the polynomial fit, we join the line to the polynomial where $K_s\text{-}4.5\mu\text{m} = 1.3$ mag. To connect the two functions we require that both the value and the first derivative of both functions be equal at $K_s\text{-}4.5\mu\text{m} = 1.3$ mag. This ensures that the attenuation correction is continuous at all points.

For Model A, we fit

$$A_J^e = \begin{cases} -0.03 + 2.58(K_s - 4.5\mu\text{m}) + 0.19(K_s - 4.5\mu\text{m})^2 & : (K_s - 4.5\mu\text{m}) \leq 1.3 \\ -0.67(K_s - 4.5\mu\text{m})^3 + 0.23(K_s - 4.5\mu\text{m})^4 & : (K_s - 4.5\mu\text{m}) \leq 1.3 \\ 1.70(K_s - 4.5\mu\text{m}) + 0.62 & : (K_s - 4.5\mu\text{m}) > 1.3 \end{cases} \quad (\text{C1})$$

$$A_H^e = \begin{cases} -0.01 + 1.62(K_s - 4.5\mu\text{m}) + 0.27(K_s - 4.5\mu\text{m})^2 & : (K_s - 4.5\mu\text{m}) \leq 1.3 \\ -0.30(K_s - 4.5\mu\text{m})^3 + 0.10(K_s - 4.5\mu\text{m})^4 & : (K_s - 4.5\mu\text{m}) \leq 1.3 \\ 1.67(K_s - 4.5\mu\text{m}) - 0.01 & : (K_s - 4.5\mu\text{m}) > 1.3 \end{cases} \quad (\text{C2})$$

$$A_{K_s}^e = \begin{cases} -0.01 + 1.04(K_s - 4.5\mu\text{m}) + 0.18(K_s - 4.5\mu\text{m})^2 & : (K_s - 4.5\mu\text{m}) \leq 1.3 \\ -0.10(K_s - 4.5\mu\text{m})^3 + 0.05(K_s - 4.5\mu\text{m})^4 & : (K_s - 4.5\mu\text{m}) \leq 1.3 \\ 1.42(K_s - 4.5\mu\text{m}) - 0.28 & : (K_s - 4.5\mu\text{m}) > 1.3 \end{cases} \quad (\text{C3})$$

For Model B, we obtain

$$A_J^e = \begin{cases} 0.70(K_s - 4.5\mu m) + 5.90(K_s - 4.5\mu m)^2 & : (K_s - 4.5\mu m) \leq 1.3 \\ -5.59(K_s - 4.5\mu m)^3 + 1.59(K_s - 4.5\mu m)^4 & : (K_s - 4.5\mu m) > 1.3 \\ 1.73(K_s - 4.5\mu m) + 0.92 & \end{cases} \quad (C4)$$

$$A_H^e = \begin{cases} -0.01 + 0.34(K_s - 4.5\mu m) + 3.93(K_s - 4.5\mu m)^2 & : (K_s - 4.5\mu m) \leq 1.3 \\ -3.15(K_s - 4.5\mu m)^3 + 0.82(K_s - 4.5\mu m)^4 & : (K_s - 4.5\mu m) > 1.3 \\ 1.75(K_s - 4.5\mu m) - 0.22 & \end{cases} \quad (C5)$$

$$A_{K_s}^e = \begin{cases} 0.19(K_s - 4.5\mu m) + 2.50(K_s - 4.5\mu m)^2 & : (K_s - 4.5\mu m) \leq 1.3 \\ -1.72(K_s - 4.5\mu m)^3 + 0.40(K_s - 4.5\mu m)^4 & : (K_s - 4.5\mu m) > 1.3 \\ 1.50(K_s - 4.5\mu m) - 0.10 & \end{cases} \quad (C6)$$